Supplementary Information For

Metallocenium Salts as Tunable Dopants for Enhanced Efficiency of Perovskite Solar Cells

Thomas Webb[†1,2], Francesco Vanin[†1,3], Danpeng Cao[3], Lei Zhu[4], William D. J. Tremlett[1], Amanz Azaden[1,2], Alice Rodgers[1,2], Polina Jacoutot[1,2], Andrew White[1], M. Saiful Islam[4], Nicholas J. Long[1], Zonglong Zhu[3*], Saif A. Haque[1,2*]

[1] Department of Chemistry and [2]Centre for Processable Electronics, Molecular Sciences Research Hub, Imperial College London, London, UK

[3] Department of Chemistry, City University of Hong Kong; Kowloon 999077, Hong Kong

[4] Department of Materials, University of Oxford, Oxford OX1 3PH, UK

[†]These authors contributed equally.

Corresponding authors: s.a.haque@imperial.ac.uk and zonglzhu@cityu.edu.hk

Methods

Sample Characterization

Preparation of Ferrocenium [Fc][Y] salts – In all cases, ferrocene (98%, Sigma-Aldrich) was reacted in excess with silver salts of a target anion (AgY) in a molar ratio (Fc: AgY = 1.05 : 1 mol). The Silver precursor salts were purchased from [BF_4] (98%, Sigma-Aldrich), [OTf](>99%, Sigma-Aldrich), [PF_6] (98%, Fluorochem), and [TFSI] (97%, Thermo Scientific). To the powders, anhydrous chloroform ($CHCl_3$, Sigma Aldrich) was added to create a solution with a concentration of 0.1 - 0.2 M. Reactions were typically conducted on a 2 mL scale. The solutions were left to stir under a nitrogen atmosphere for 12 hours. In all cases, the solution changed colour from orange to dark blue /black and the formation of metallic silver could be seen on the base of the vials. For [BF_4],[OTf] and [TFSI], the blue product solution was filtered through a 0.2 μm PTFE filter (VWR) and combined with anhydrous and degassed diethyl ether (1:7 v/v) (DEE, Acros Organics, 99.8 %). The solution was rotary evaporated until the formation of needle crystals was observed. The solution was cooled overnight in at 5 °C and submerged in an ice bath before removing the solid crystals from the solution. The crystals were washed a minimum of 3 times using diethyl ether or until the DEE washes came out colourless and a final wash of *n*-hexane. The collected solids were dried under vacuum. In the case of [Fc][PF_6] a precipitation reaction was observed forming blue powder during the reaction between Fc and $AgPF_6$. The solid was removed, redissolved in isopropyl alcohol, filtered and recrystallised to afford small black crystals.

Ferrocenium tetrafluoroborate - **[Fc][BF_4]**: yield: 62 %, **MS** m/z calcd. for $[Fe(C_5H_5)_2]^+$ m/z 186.0132; found 186.0135, m/z calcd. for $[BF_4]^-$ 87.0029; found 87.0031, **^{1}H** {$CDCl_3$, 293 K, 400 MHz} δ 32.5 (s, broad), **^{19}F** {$CDCl_3$, 293 K, 400 MHz} δ -175.9, ppm (s), **FTIR** ν 1028 (s, B-F stretch), 1001 cm^{-1} (s, B-F stretch).

Ferrocenium trifluoromethanesulfomate - **[Fc][OTf]**: yield 68 %, **MS** m/z calcd. for $[Fe(C_5H_5)_2]^+$ m/z 186.0132; found 186.0135, m/z calcd. for $[OTf]^-$ 148.9520 ; found 148.9520. **^{1}H** {$CDCl_3$, 293 K, 400 MHz} δ 31.8 (s, broad), **^{19}F** {$CDCl_3$, 293 K, 400 MHz} δ -91.8 ppm (s). **FTIR** ν 1255 (s, S = O, stretch) , 1153 cm^{-1} (s, C-F stretch).

Ferrocenium hexafluorophosphate - **[Fc][PF_6]**: Yield 73 %, **MS** m/z calcd. for $[Fe(C_5H_5)_2]^+$ m/z 186.0132; found 186.0127, m/z calcd. for $[PF_6]^+$ 144.9642; found 144.9639. **^{1}H** {$(CD_3)_2CO$, 293 K, 400 MHz} δ 32.8 (s, broad), **^{19}F** {$(CD_3)_2CO$, 293 K, 400 MHz} δ -75.5 ppm (d, $J_{FP}{}^1$ = 760 Hz). **FTIR** ν 809 cm^{-1} (s, P-F stretch)

Ferrocenium bis(trifluoromethylsulfonimide) - **[Fc][TFSI]:** yield 65 %, **MS** m/z calcd. for $[Fe(C_5H_5)_2]^+$ m/z 186.0132; found 186.0127, m/z calcd. for $[TFSI]^-$ 279.92; found 279.92. **^{1}H** {$CDCl_3$, 293 K, 400 MHz} 32.8 (s, broad), **^{19}F** {$CDCl_3$, 293 K, 400 MHz} δ -88.8 ppm (s). **FTIR** ν 1343 & 1048 cm^{-1} (s, S=O stretches), 1185 cm^{-1} (s, C-F stretch).

The X-ray crystal structure of [Fc][TFSI]

Crystal data for **[Fc][TFSI]**: $C_2F_6NO_4S_2 \cdot C_{10}H_{10}Fe$, M = 466.18, monoclinic, P_{21}/n (no. 14), a = 16.3394(5), b = 14.4078(3), c = 16.6288(6) Å, β = 119.316(4)°, V = 3413.3(2) Å3, Z = 8 [two independent complexes], Dc = 1.814 g cm^{-3}, $\mu(M_o\text{-}K_\alpha)$ = 1.209 mm^{-1}, T = 173 K, black blocks, Agilent Xcalibur 3E diffractometer; 7671 independent measured reflections (Rint = 0.0511), F2 refinement,[X1,X2,X3] R_1(obs) = 0.0496, wR_2(all) = 0.1167, 5379 independent observed absorption-corrected reflections [$|F_o| > 4\sigma(|Fo|)$, completeness to θ full(25.2°) = 99.9%], 557 parameters. CCDC 2479149.

The structure of FcTFSI was found to contain two crystallographically independent [Fc][TFSI] pairs. The C6-based Cp ring, the whole of the Fe2-based ferrocene unit, and the whole of the N51-based TFSI moiety were all found to be disordered. For the C6-based Cp ring and the N51-based TFSI moiety two orientations were identified of ca. 70:30 and 75:35% occupancy respectively, their geometries were optimised, the thermal parameters of adjacent atoms were restrained to be similar, and only the non-hydrogen atoms of the major occupancy orientations were refined anisotropically (those of the minor occupancy orientations were refined isotropically). For the Fe2-based ferrocene unit two orientations were identified of ca. 64 and 365% occupancy, their geometries were optimised, the thermal parameters of adjacent atoms were restrained to be similar, and only the non-hydrogen atoms of the major occupancy orientation, and the iron atom of the minor occupancy orientation, were refined anisotropically (the remaining atoms of the minor occupancy orientation were refined isotropically).

Preparation of Ferrocenium [M($C_{10}H_{10-n}(X)_n$][TFSI] salts:

The synthesis of [$Fc(Me)_2$], [Cc] and [Nc] followed the process outline above, using $Fc(Me)_2$ (97%, Thermo Scientific), Cc (98%, Thermo scientific) and Nc (98%, Fisher scientific) as starting materials.The reaction of [Fc(COOH)] and [$Fc(I)_2$] salts was prepared through combining either Fc(COOH) (97%, Sigma-Aldrich) or $Fc(I)_2$ with AgTFSI in a molar ratio (Fc(X): AgTFSI = 1.05 : 1 mol). The solid formed during the precipitation was removed from the solvent under N_2 and redissolved in diethyl ether. The solution was filtered, rotary evaporated, the solid extracted, and chloroform was also used to encourage crystallisation, yielding a black powder of small crystalline clusters. The [Fc(COOH)] and [$Fc(I)_2$] powders were washed in chloroform. [$Fc(Br)_2$] was prepared via direct reaction between $Fc(Br)_2$ (97%, Sigma-Aldrich) and AgTFSI under N_2 at 0.2 M concentration. The reaction solution was left to stir overnight and turned a dark blue / green. The solution was filtered and to the solution DEE antisolvent was slowly added (1:10 v/V). The solution was evaporated *in vacuo* to the point fine needles began to form at the bottom of the glassware and the solution was refrigerated, before being submerged in an ice bath. After 24 hours long blue needles of [$Fc(Br_2)$][TFSI] were

formed, suspended in a green solution. The crystals were washed using diethyl ether and *n*-hexane and dried under vacuum.

1,1'-dimethlylferrocenium bis(trifluoromethylsulfonimide) - **[Fc(Me)$_2$][TFSI]**: yield 63 %, **MS** m/z calcd. for [Fc(Me)$_2$]$^+$ 214.0445; found 214.0435, m/z cald. for [TFSI]$^-$ -279.9173; found -279.9177. **^{1}H** {$CDCl_3$, 293 K, 400 MHz} δ 35.5 (s, broad), 31.6 ppm (s, broad), **^{19}F** {$CDCl_3$, 293 K, 400 MHz} δ 85.0 ppm (s). **FTIR** ν 1343 & 1048 cm^{-1} (s, S=O stretches), 1185 cm^{-1} (s, C-F stretch).

Ferroceniumcarboxylic acid bis(trifluoromethylsulfonimide) – **[Fc(COOH)][TFSI]**: yield 47 %, **MS** m/z calcd. for [FcCOOH)]$^+$ 230.0030; found 230.0022, m/z calcd. for [TFSI]$^-$ -279.9173; found -279.9177. **FTIR** ν 1698 cm^{-1} (s, C=O stretch), 1292 cm^{-1} (s, C-O stretch), 1343 & 1048 cm^{-1} (s, S=O stretches), 1185 cm^{-1} (s, C-F stretch).

1,1'-diiodoferroceneium bis(trifluoromethylsulfonimide) – **[Fc(I)$_2$][TFSI]**: Yield 52 %, **MS** m/z calcd. for [Fc(I)$_2$]$^+$ 437.8065; found 437.8057, m/z calcd. for [TFSI]$^-$ 279.9173; found 279.9171. **^{1}H** {($CDCl_3$ + DCM), 293 K, 400 MHz} δ 26.4 (s, broad), 22.4 (s, broad), **^{19}F** {(($CDCl_3$ + DCM), 293 K, 400 MHz} δ 84.8 ppm (s). **FTIR** ν 1348 & 1048 cm^{-1} (s, S=O stretches), 1181 cm^{-1} (s, C-F stretch).

1,1'-dibromoferrocenium bis(trifluoromethylonimide) – **[Fc(Br)$_2$][TFSI]**: Yield 81 %, **MS** m/z calcd. for [Fc(Br)$_2$]$^+$ 343.83; found 343.83, m/z calcd for [TFSI]$^-$ 279.91; found 279.9171. **^{1}H** {$CDCl_3$, 293 K, 400 MHz} δ 33.09 (s, broad), 29.9 (s, broad) **^{19}F** {$CDCl_3$, 293 K, 400 MHz} δ 85.5 ppm (s). **FTIR** ν 1348 & 1048 cm^{-1} (s, S=O stretches), 1181 cm^{-1} (s, C-F stretch).

Cobaltocenium bis(trifluoromethylonimide) – **[Cc][TFSI]**: Yield 77 %, **MS** m/z calcd. for [Cc]$^+$ 189.0114; found 189.0107, m/z calcd for [TFSI]$^-$ 279.9173; found 279.9163. **^{1}H** { $CDCl_3$, 293 K, 400 MHz} δ 5.7 ppm (s), **^{19}F** { $CDCl_3$, 293 K, 400 MHz} -78.8 ppm (s).

Nickelocenium bis(trifluoromethylonimide) – **[Nc][TFSI]**: Yield 65 %, **MS** m/z calcd. for [Nc]$^+$ 188.01; found 188.01, m/z calcd for [TFSI]$^-$ 279.91; found 279.91. **^{1}H** {$CDCl_3$, 293 K, 400 MHz} δ -104 ppm (s, broad), **^{19}F** {$CDCl_3$ + DCM, 293 K, 400 MHz} δ -75.7 ppm (s). **FTIR** ν 1348 & 1048 cm^{-1} (s, S=O stretches), 1181 cm^{-1} (s, C-F stretch).

Note:

Despite the acceptable yields (>50%) achieved using the current synthetic approach we note that several synthetic routes are known to oxidized ferroceniums with varying counterions and substitutions.[1,2] Furthermore, it is well understood that ferrocenium substitution and counterions selection both play a significant role in the yields achievable with different synthetic methods.

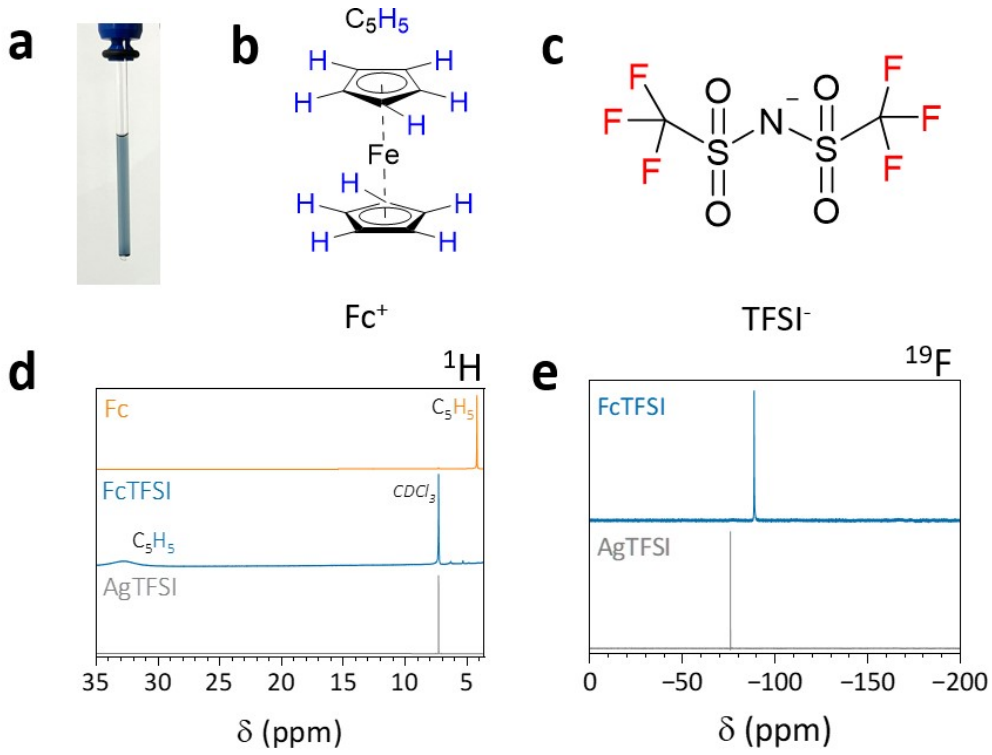

Supplementary Figure S1. Nuclear magnetic resonance (NMR) spectroscopy on the synthesis of ferrocenium bis(trifluoromethylsulfonimide) ([Fc][TFSI]) **a**, Photograph of [Fc][TFSI] dissolved in $CDCl_3$, **b**, Chemical structure showing ^{1}H environments in the Fc/Fc^{+} cation, **c**, Chemical structure showing ^{19}F environments in $TFSI^{-}$ anion. **d**, ^{1}H NMR spectra of ferrocene, [Fc][TFSI] and AgTFSI, showing a strong downfield shift to ~33 ppm associated with Fc^{+}. **e**, ^{19}F NMR showing a shift in the CF_3 environment of $TFSI^{-}$ following reaction of the silver to FcTFSI.

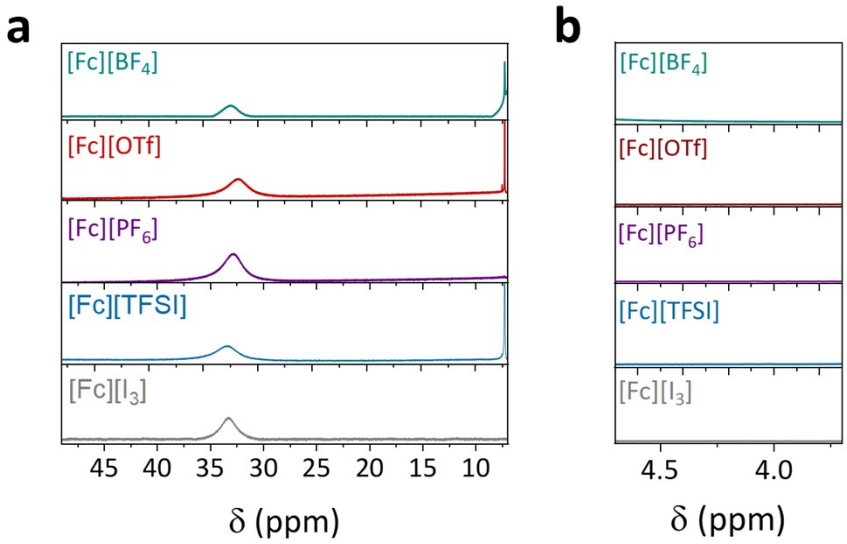

Supplementary Figure S2. ^{1}H NMR spectroscopy confirming the oxidation of ferrocene with different silver salts, all salts were dissolved in $CDCl_3$ except for $[Fc][PF_6]$, which was measured in d6-acetone . **a**, Regions associated with the cyclopentadienyl (Cp) ring protons showing the Fe^{3+} oxidation state was formed. **b**, Region associated with the peak of neutral ferrocene Cp ring protons showing that all ferrocene reactant was used up during the reaction.

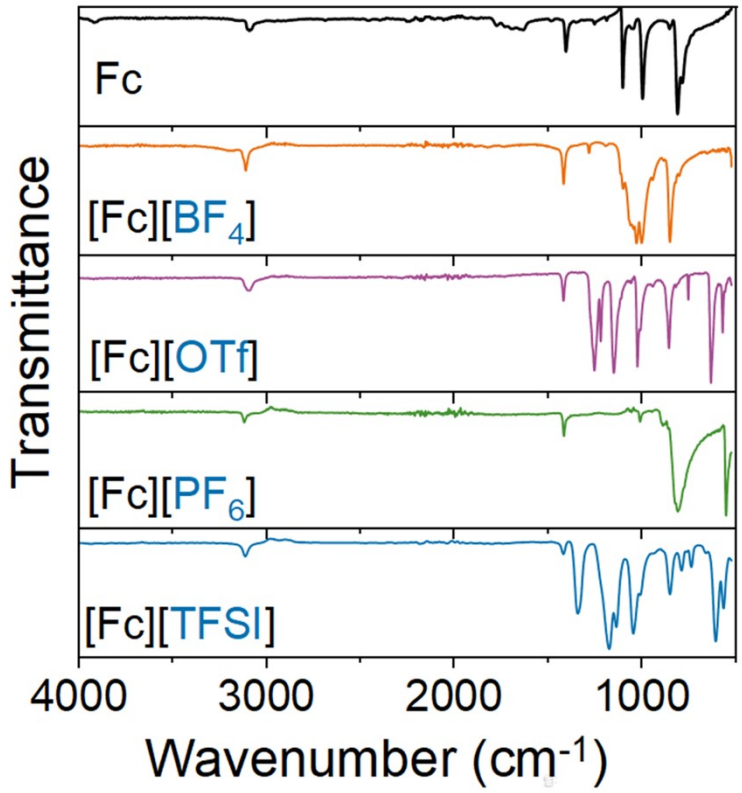

Supplementary Figure S3. Attenuated Total Reflectance Fourier-Transform Infrared (ATR-FTIR) spectroscopy on ferrocenium salts showing characteristic stretches of the anions at $\nu < 2000\ cm^{-1}$.

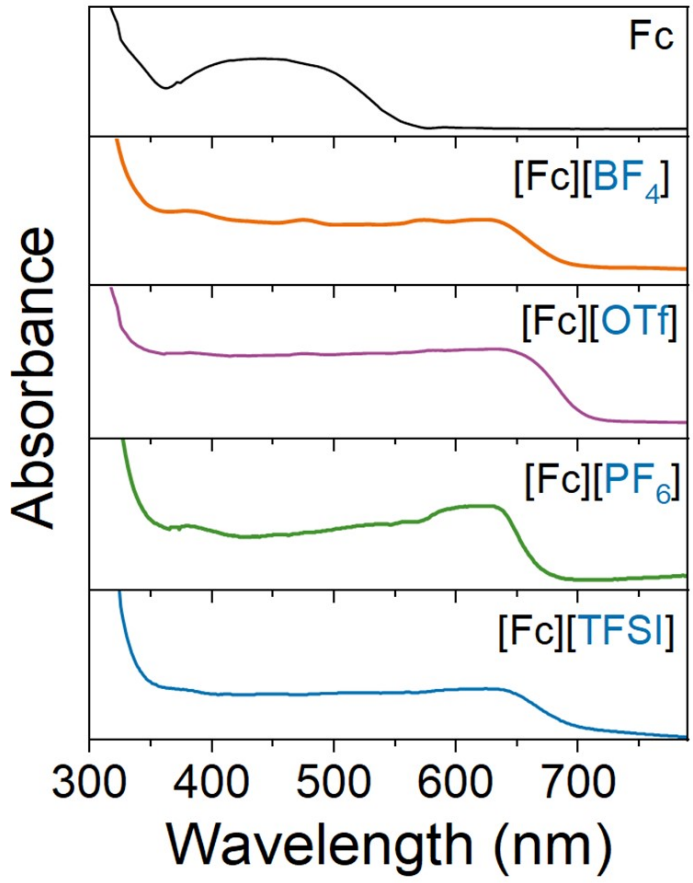

Supplementary Figure S4. Solid-state UV-visible absorbance spectra of different ferrocenium salts collected between microscope slides. Spectra show a significant red-shift in the absorbance profile upon oxidation with respect to ferrocene.

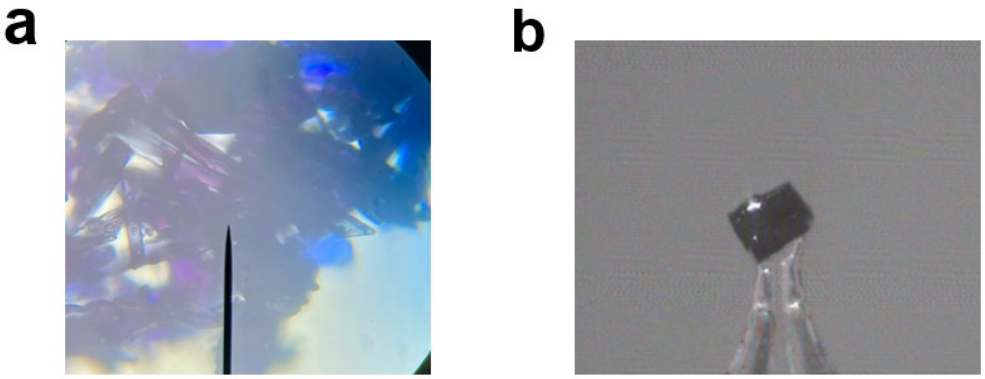

Supplementary Figure S5. Microscope images of FcTFSI crystals. **a**, Photograph under 10x magnification. **b**, Image of crystal used for single-crystal X-ray diffraction (XRD) measurements.

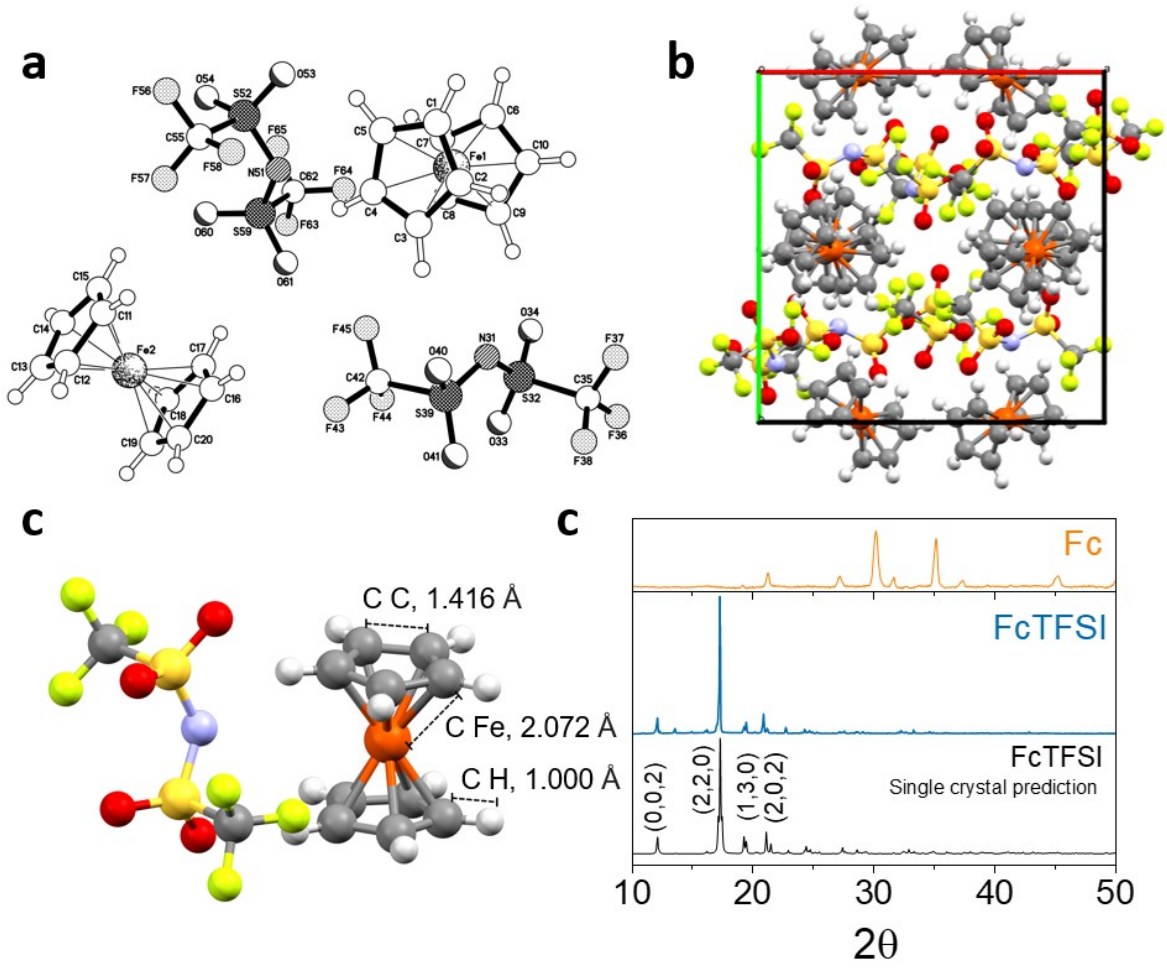

Supplementary Figure S6. Crystallographic data on [Fc][TFSI]. **a**, Graphic of [Fc][TFSI] crystal structure created using the SCXRD data. **b**, [Fc][TFSI] unit cell projection along the *c* crystallographic axis. **c**, [Fc][TFSI] molecule showing the interatomic distances in Fc^{+}. **d**, Powder x-ray diffraction patterns of ferrocene, [Fc][TFSI] and the predicted [Fc][TFSI] powder pattern from the SCXRD crystal unit cell.

Table S1. Crystallographic properties of [Fc][TFSI] determined from SCXRD measurements.

Space Group	$P2_1/n(14)$
Z	8
(a,b,c)	16.339 Å, 14.407 Å, 16.628 Å
α , β, γ	α = 90.0 °, β = 119.3 °, γ = 90.0 °
Cell Volume (V)	3413 Å

Supplementary Figure S7. Photographs of spiro-OMeTAD solutions in chlorobenzene (90 mg ml^{-1}) prepared using ferrocenium doping with different anions from left to right: [Fc][OTf], [Fc][BF_4], [Fc][TFSI], [Fc][I_3],[Fc][PF_6].

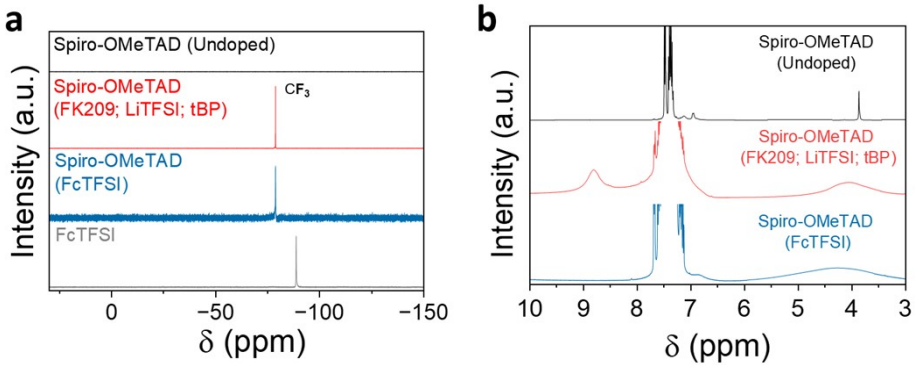

Supplementary Figure S8. Nuclear Magnetic Resonance spectroscopy showing the changes to spiro-OMeTAD after doping with [Fc][TFSI]. **a**, ^{19}F NMR spectra of the TFSI anion in spiro-OMeTAD doped using conventional FK209 and LiTFSI, spiro-OMeTAD doped with [Fc][TFSI] and the reference shift of [Fc][TFSI]. From the spectra we report that the same [spiro-OMeTAD][TFSI] is produced when doping with [Fc][TFSI] or FK209 / LiTFSI. **b**, ^{1}H NMR spectra of spiro-OMeTAD without doping (black), conventional FK209 + LiTFSI doping (red) and doping with [Fc][TFSI] (blue).

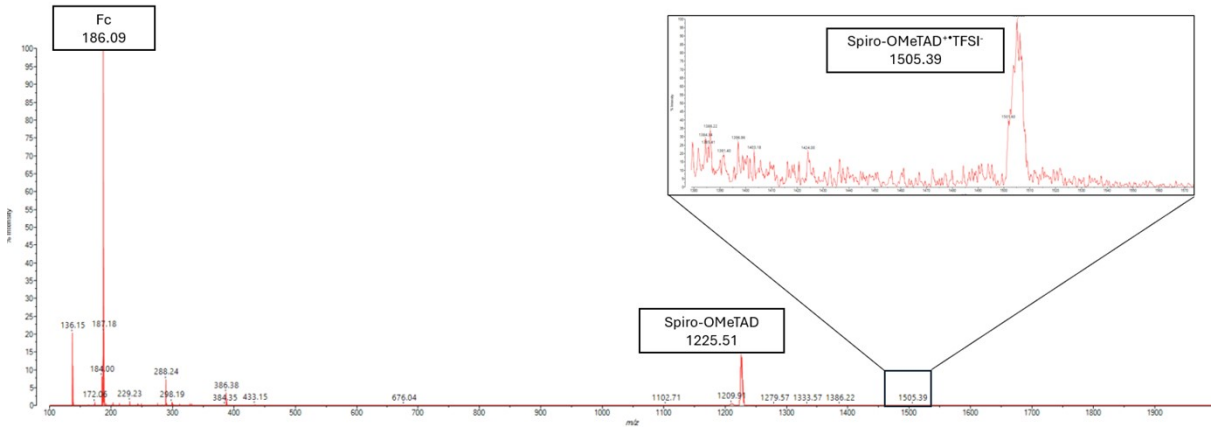

Supplementary Figure S9. Matrix-Assisted Laser Desorption/Ionisation (MALDI) Time of Flight spectrometry on spiro-OMeTAD doped with [Fc][TFSI] showing the formation of spiro-OMeTAD$^{+\bullet}$TFSI and reformation of Fc. [Fc][TFSI] is below detection following doping with a calcd. mass expected at 466.18. We note that the comparison of the relative concentrations is greatly affected by the presence of ions. EPR provides a more accurate estimate of the ratio of spiro-OMeTAD to spiro-OMeTAD$^{+\bullet}$.

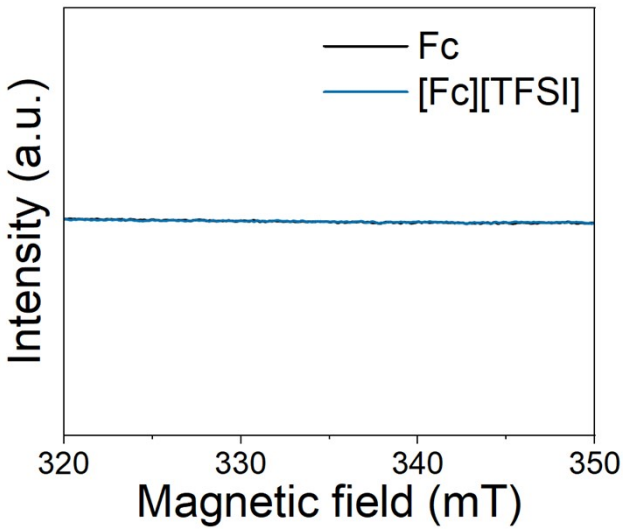

Supplementary Figure S10. Electron Paramagnetic Resonance (EPR) spectra of ferrocene and [Fc][TFSI] powders dissolved in chloroform, measured as 298 K. No signal observed as a consequence of fast spin relaxation times in [Fc][TFSI].

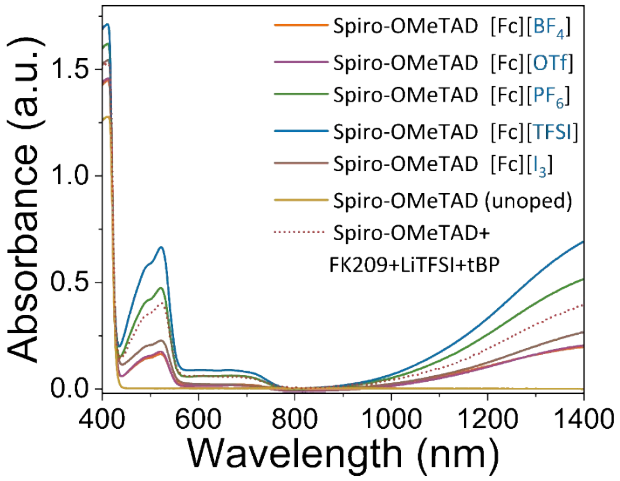

Supplementary Figure S11. UV-visible absorbance spectroscopy on spiro-OMeTAD solution doped with ferrocenium salts of differing anions.

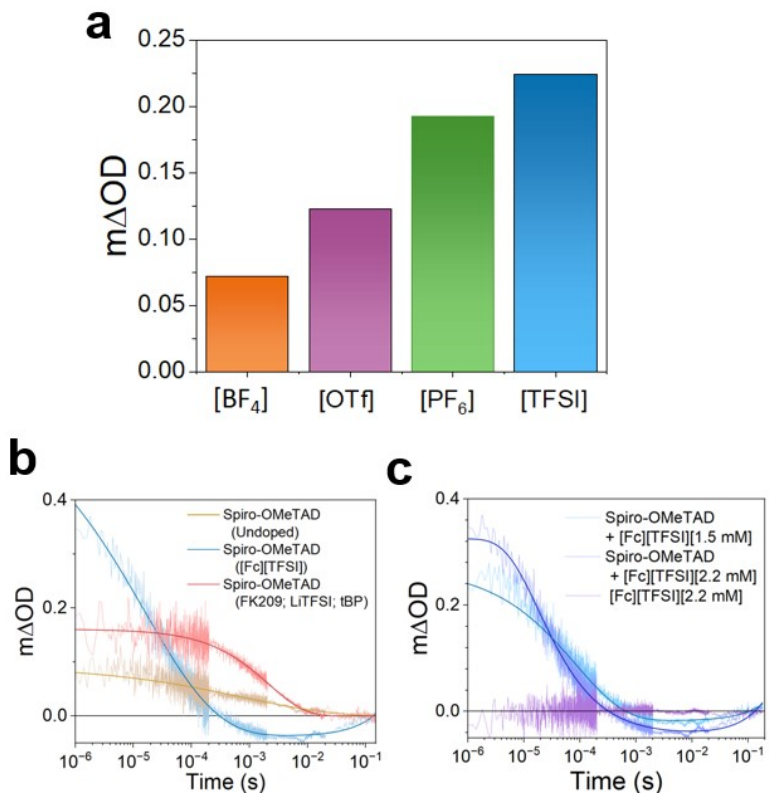

Supplementary Figure S12. Supplementary TAS data; **a**, Bar chart comparing between anions [Y^-] of the $m\Delta OD_{max,}$ which corresponds to the maximum yield of hole transfer, and is defined as the change in optical density (mΔOD) at 1 μs. **b**, TAS decays comparing the spectral shape and $m\Delta OD_{max}$ between [Fc][TFSI] and LiTFSI based dopanats. **c**, Figure to determine the [Fc][TFSI], when applied to spiro-OMeTAD HTL, as the origin of the changed kinetics and greater yield of hole transfer. Control of [Fc][TFSI] solid sample to show no unexpected transient signals directly from the dopant.

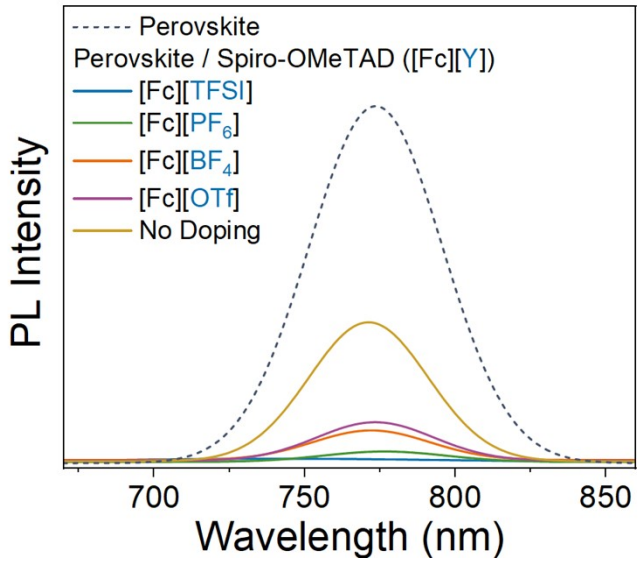

Supplementary Figure S13. Photoluminesence (PL) spectroscopy of perovskite without and with spiro-OMeTAD as HTL hole quench. Spiro-OMeTAD doped with different ferrocenium salts to compare the hole extraction performance as a function of anion.

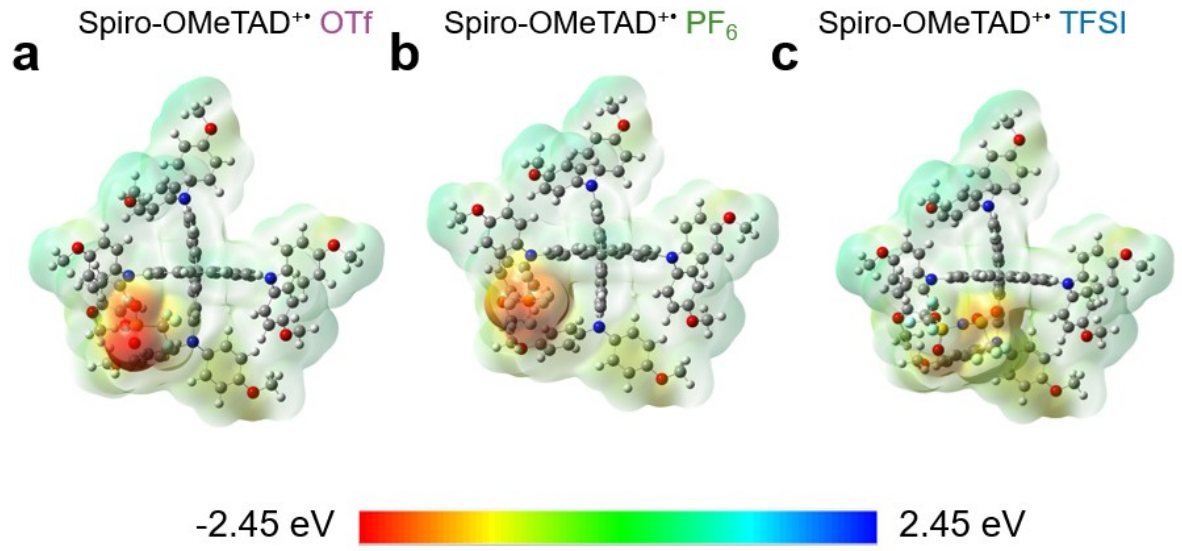

Supplementary Figure S14. Comparison of the electronic surface potential (ESP) maps of the spiro-OMeTAD^{+}Y^{-}doped salts. Dark red regions correspond to regions of increased negative charge (electron density).

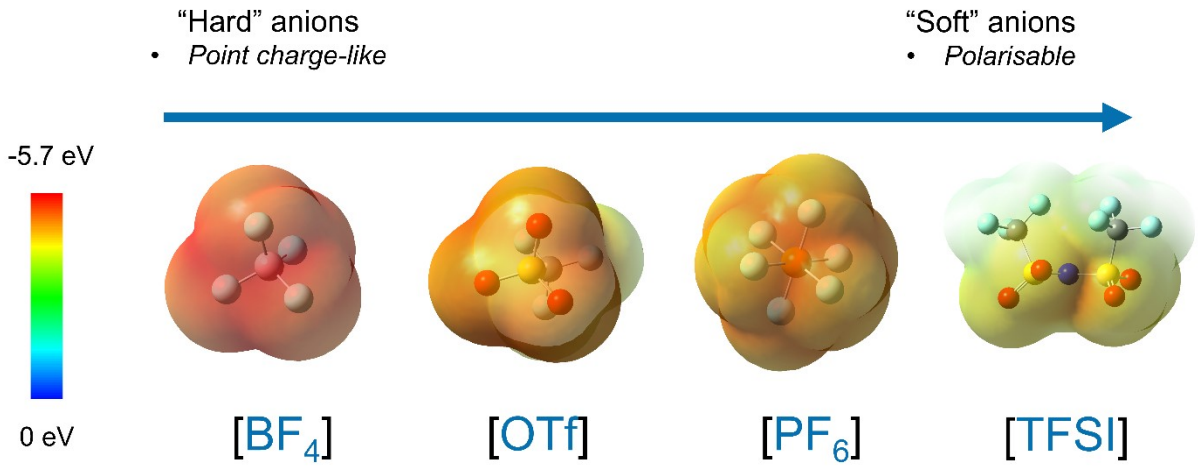

Supplementary Figure S15. Comparison of the electronic surface potential (ESP) across different ferrocenium counter anions used to dope spiro-OMeTAD. Smaller, harder cations such as BF_4 correlate to poorer performance, while more polarizable anions such as TFSI yield greater doping and improved performance.

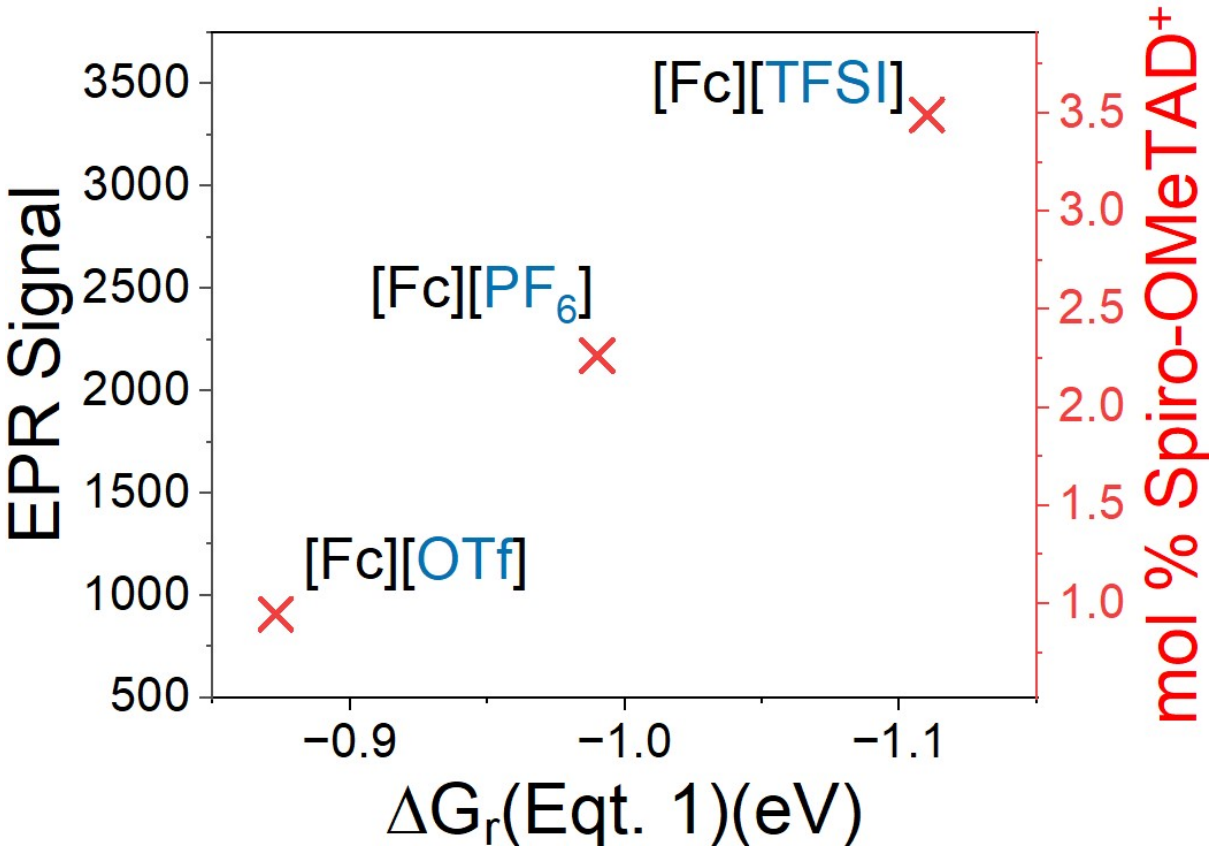

Supplementary Figure S16. Comparison between the DFT prediction of the Gibbs free reaction energy (ΔG_r) of the proposed doping mechanism and the experimentally measured EPR signal of the spiro-OMeTAD solution and the corresponding molar concentration of spiro-$OMeTAD^{+\bullet}$.

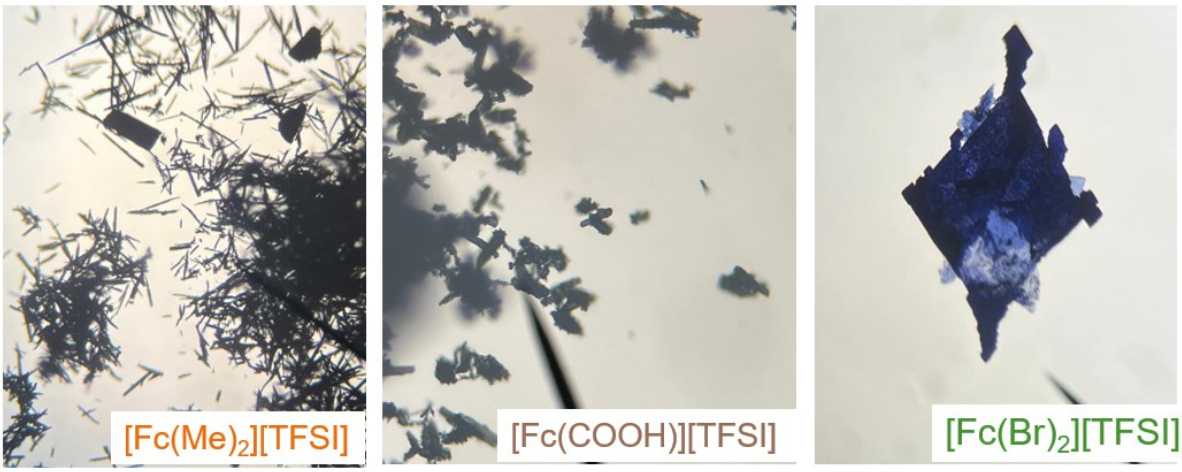

Supplementary Figure S17. Microscope images of a selection of ferrocenium salts ([$Fc(Me)_2$][TFSI], [Fc(COOH)][TFSI] and [$Fc(Br)_2$][TFSI]) chosen for recrystallisation. [$Fc(I)_2$][TFSI] formed a black powder similar to [Fc(COOH)][TFSI].

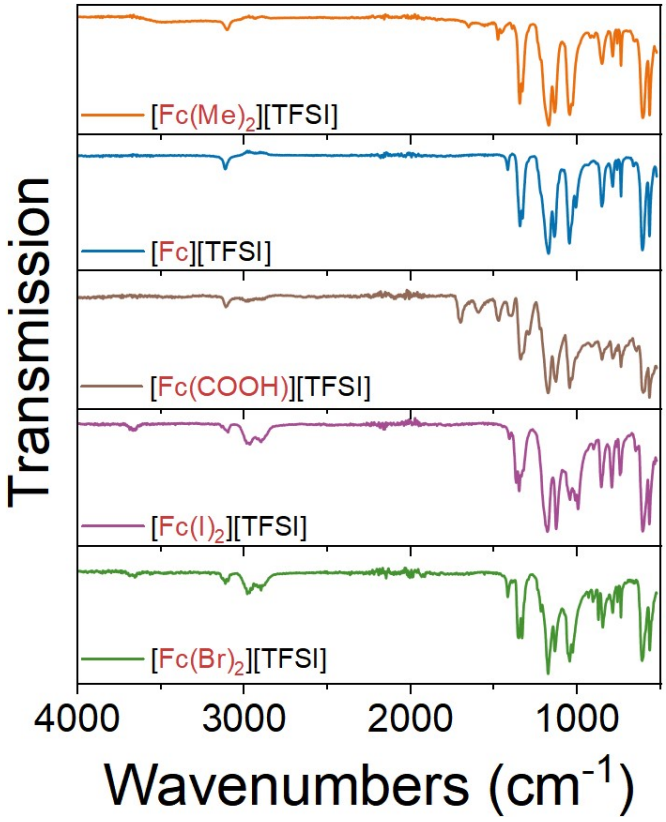

Supplementary Figure S18. ATR-FTIR spectra of bis(trifluoromethylsulfonimide) (TFSI) ferrocenium salts with different functionality on the cyclopentadienyl groups.

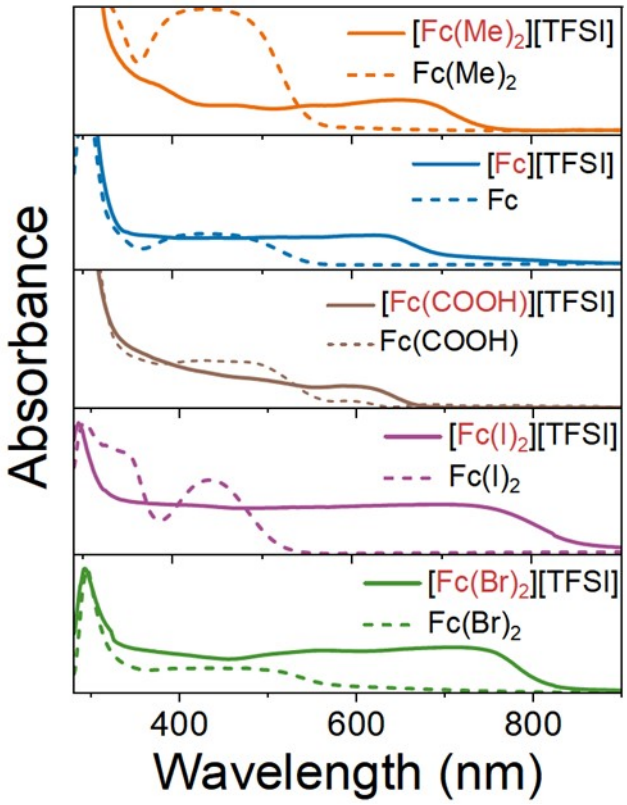

Supplementary Figure S19. UV-visible absorbance spectra of studied ferrocene derivatives and the oxidised ferrocenium bis(trifluoromethylsulfonimide) [TFSI] salt.

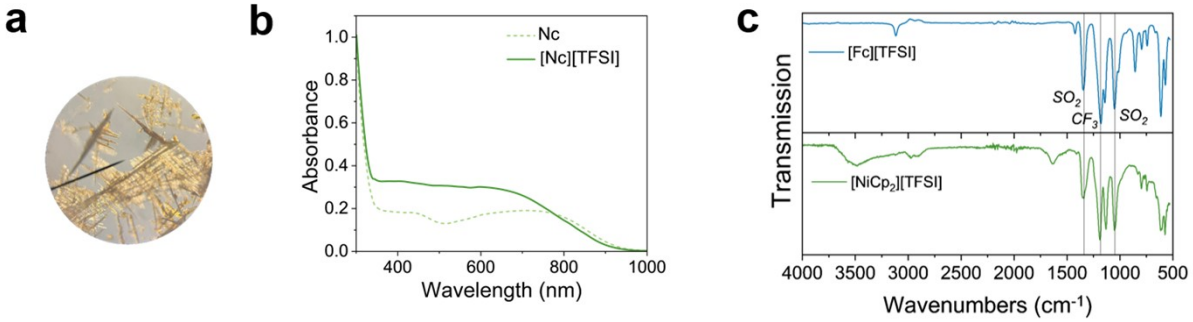

Supplementary Figure S20. Characterisation of nickeloceneium bis(trifluoromethylsulfimide) [Nc][TFSI], **a**, Microscope image of brown [Nc][TFSI] crystals, where unreacted Nc is dark green. **b**, UV-visible absorbance spectra of [Nc][TFSI] oxidised salt compared to the Nc starting material. **c,** ATR-FTIR spectra comparing [Fc][TFSI] as a TFSI reference with [Nc][TFSI] showing the same -SO_2 and -CF_3 stretching modes.

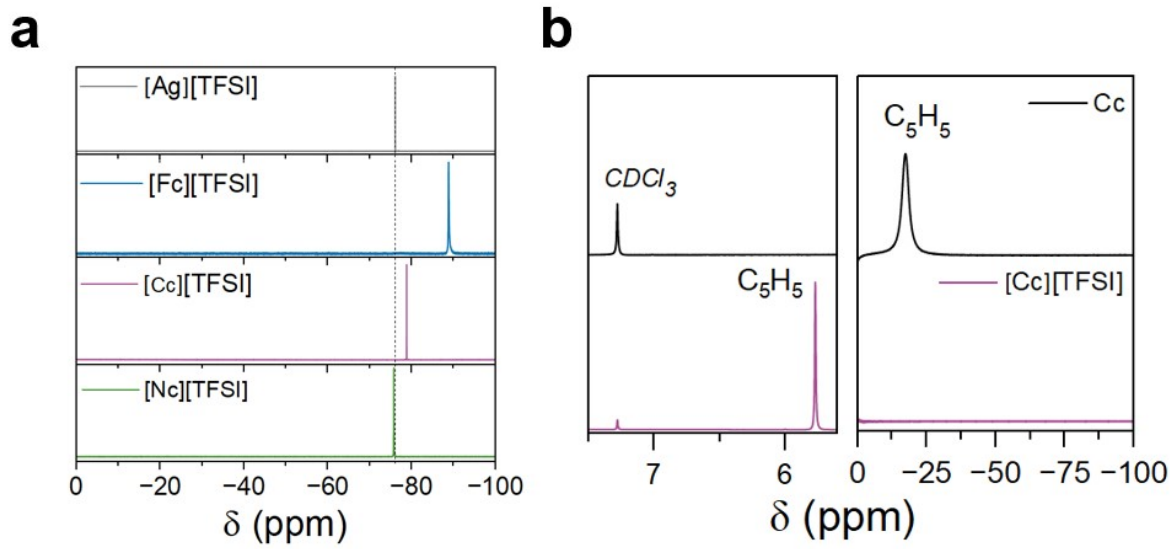

Supplementary Figure S21. a, Comparison of the TFSI ^{19}F NMR chemical environments when producing TFSI salts of different metal ions. **b**, ^{1}H NMR of Cc before oxidation with AgTFSI (black) and post-oxidation ([Cc][TFSI])(purple). The Cp ring singlet transitions significantly upfield following oxidation of the cobaltocene to cobaltocenium .

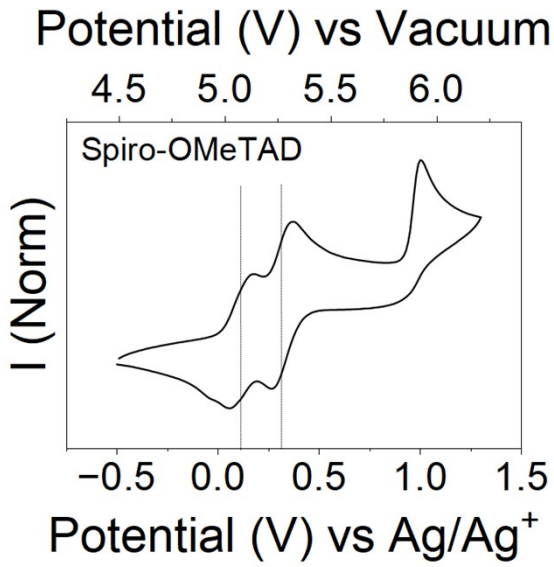

Supplementary Figure S22. Cyclic Voltammetry measurement of spiro-OMeTAD 2mM solution in [NBu_4PF_6] 0.15 M dissolved in acetonitrile. Solution scanned at 100 mV/s, first two half-wave potentials corresponding to the first two oxidation states of spiro-OMeTAD are indicated.

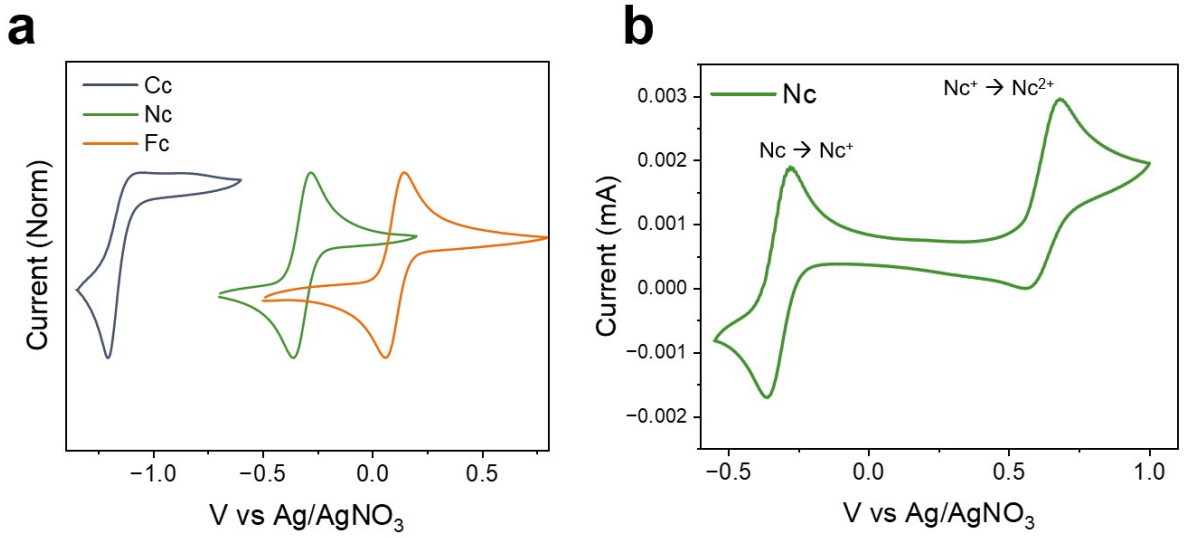

Supplementary Figure S23. a, Cyclic voltammogram of ferrocene, cobaltocene, nickelocene dissolved in ACN $nBuPF_6$ electrolyte measured at a scan rate of 100 mV/s. First oxidation state of nickelocene occurs at -0.32 V and cobaltocene -1.14 V w.r.t $Ag/AgNO_3$ reference. **b**, Nc first and second oxidation potentials.

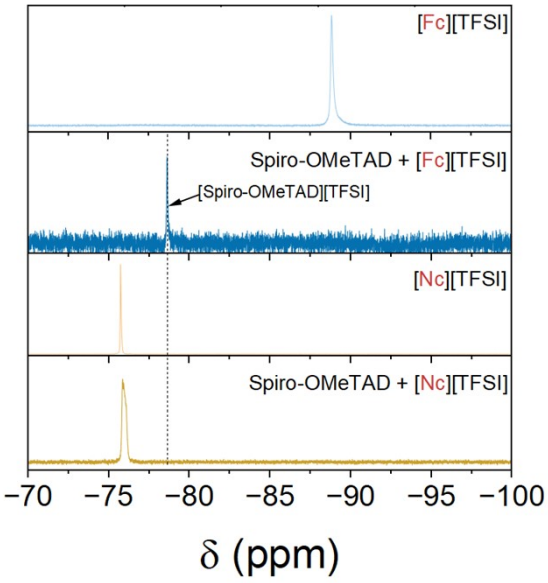

Supplementary Figure S24. ^{19}F NMR data probing the TFSI cations during ion exchange. [Fc][TFSI] undergoes ion exchange with spiro-OMeTAD to form [spiro-OMeTAD][TFSI], changing the chemical shift of the TFSI ($-CF_3$) groups. Spiro-OMeTAD prepared with nickel-based [Nc][TFSI] does not produce [spiro-OMeTAD][TFSI] owing to the lower oxidation potential of the nickelocenium, which is insufficient to promote oxidation of spiro-OMeTAD to spiro-$OMeTAD^+$

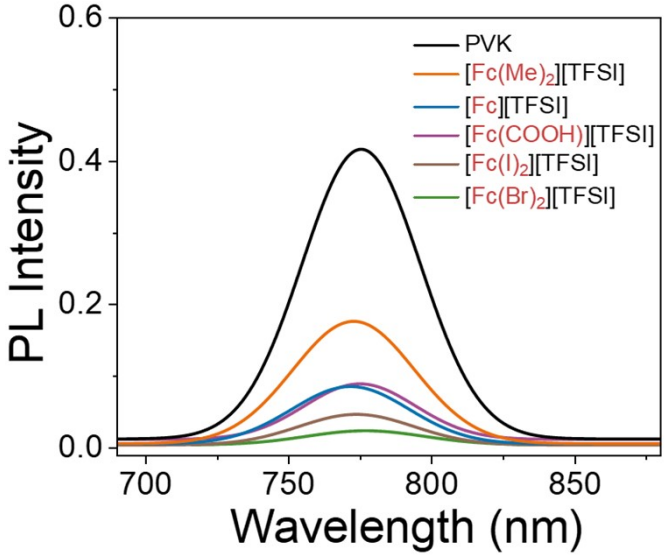

Supplementary Figure S25. Photoluminescence spectra of pristine perovskite (black) and perovskite with a spiro-OMeTAD HTL doped with different ferrocenium salt dopants.

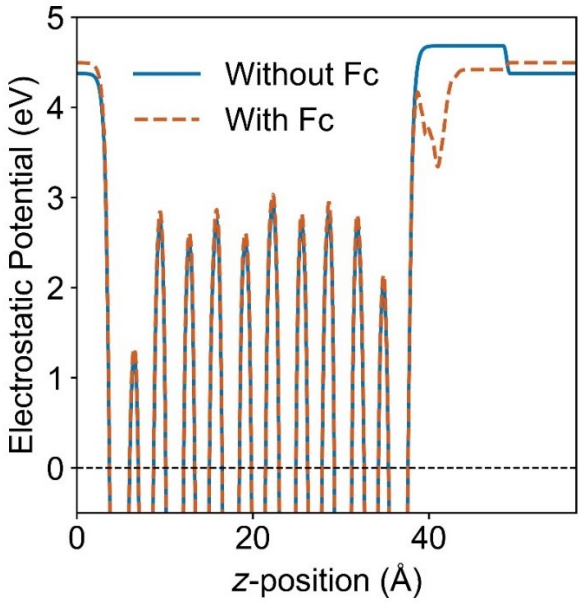

Supplementary Figure S26: Planar-averaged electrostatic potential along the surface-normal (z) direction for the MAPbI3 (001) PbI2-terminiated surface, with (orange dashed line) and without ferrocene (blue line) near the surface, processed using VASPKIT (ref.). The vacuum levels are taken at $z = 47.5$. (ref. V. WANG, N. XU, J.-C. LIU, G. TANG, W.-T. GENG, VASPKIT: A User-Friendly Interface Facilitating High-Throughput Computing and Analysis Using VASP Code, Computer Physics Communications 267, 108033, (2021), DOI: 10.1016/j.cpc.2021.108033)

Supplementary Table S2: Calculated surface vacuum level (E_{vac}), surface Fermi energies (E_{Fermi}), and predicted work function (Φ).

	E_{vac}	E_{Fermi}	Φ
Without Fc	4.68	-0.98	5.67
With Fc	4.42	-0.24	4.66
$\Delta\Phi$			-1.01

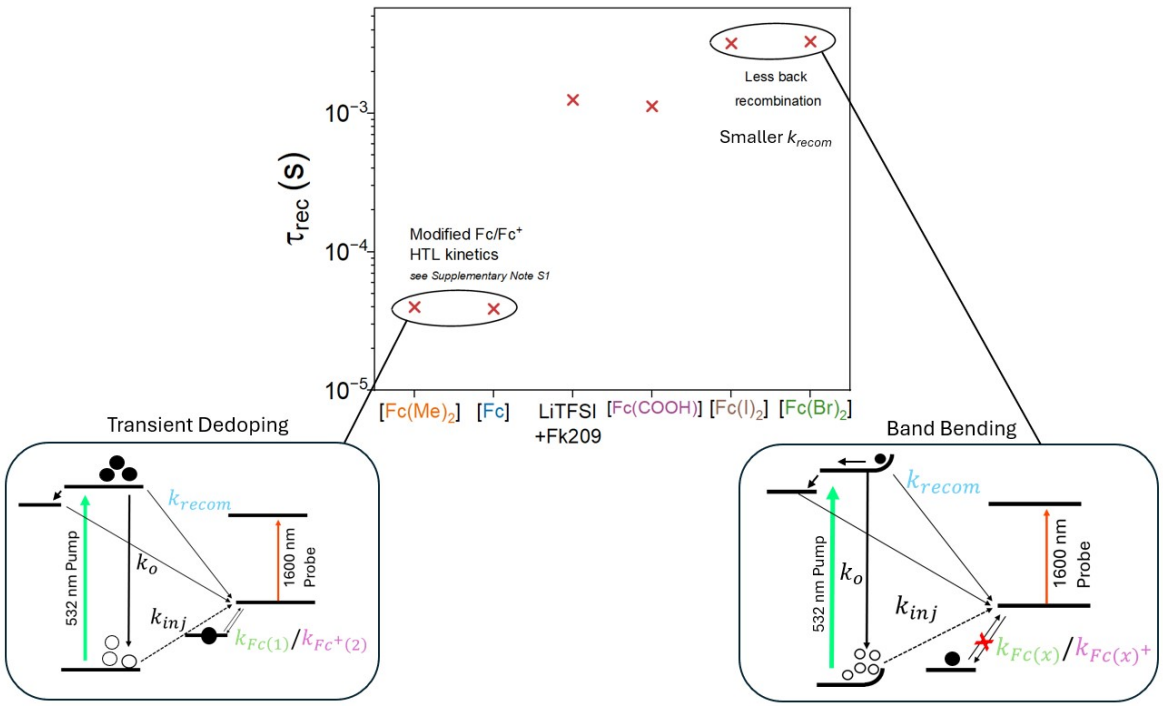

Supplementary Figure S27: Comparison of the TAS decay lifetimes recorded of the hole polaron in spiro-OMeTAD with different ferroceneium bis(trifluoromethylsulfonimide) dopants. In ferrocenium cations with lower E_{ox}; $[Fc(Me)_2]$ and [Fc] the lifetime is shortened with respect to LiTFSI and FK209 doping, resulting from transient Dedoping effects discussed in *Supplementary Note 1*. Doping with more oxidising ferrocenium cations; $[Fc(I)_2]$ and $[Fc(Br)_2]$ the transient de-doping effects are avoided by *via* establishing a potential barrier to de-doping. In this scenario, band bending effects dominate which direct electrons away from the HTL interface and generating longer lifetimes in the TAS decays.

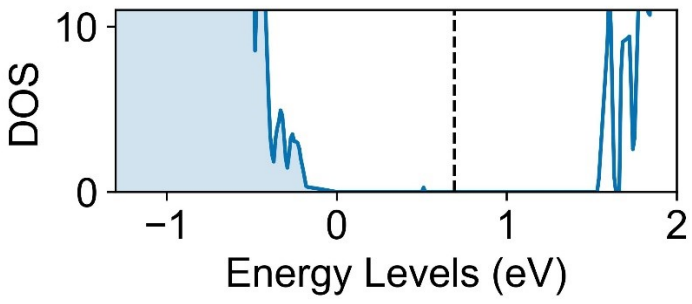

Supplementary Figure S28: Calculated electronic density of states (DOS) for the $MAPbI_3$ surface with Fc doping. DOS is projected onto atoms in the three middle layers located one layer below the surface. The DOS is aligned to the surface VBM, set to zero on the energy axis. The black dashed line indicates the position of the highest occupied level at the surface.

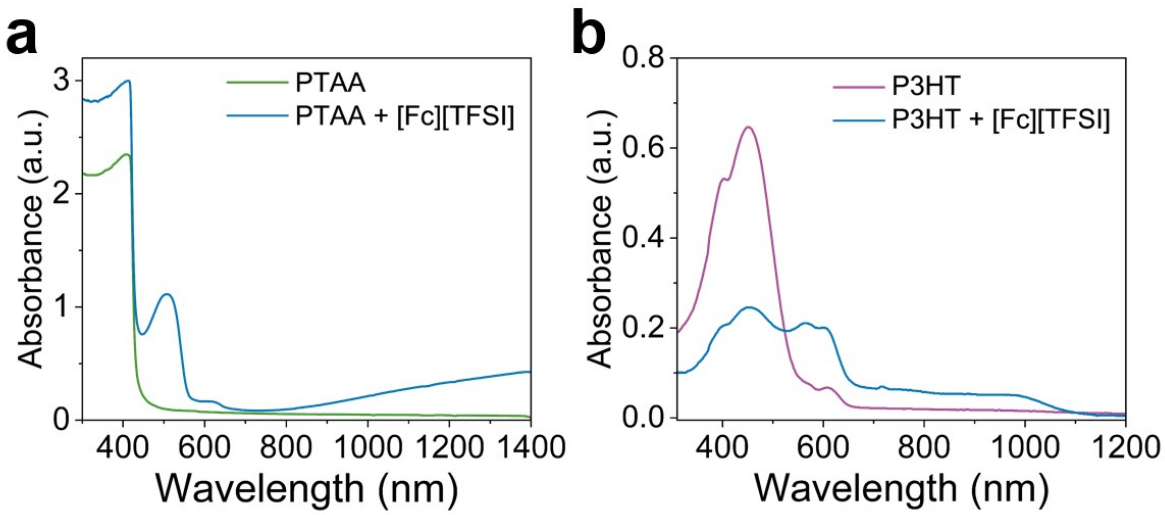

Supplementary Figure S29. UV-visible absorbance spectra of **a**, PTAA, PTAA + [Fc][TFSI], and **b**, P3HT, P3HT + [Fc][TFS]

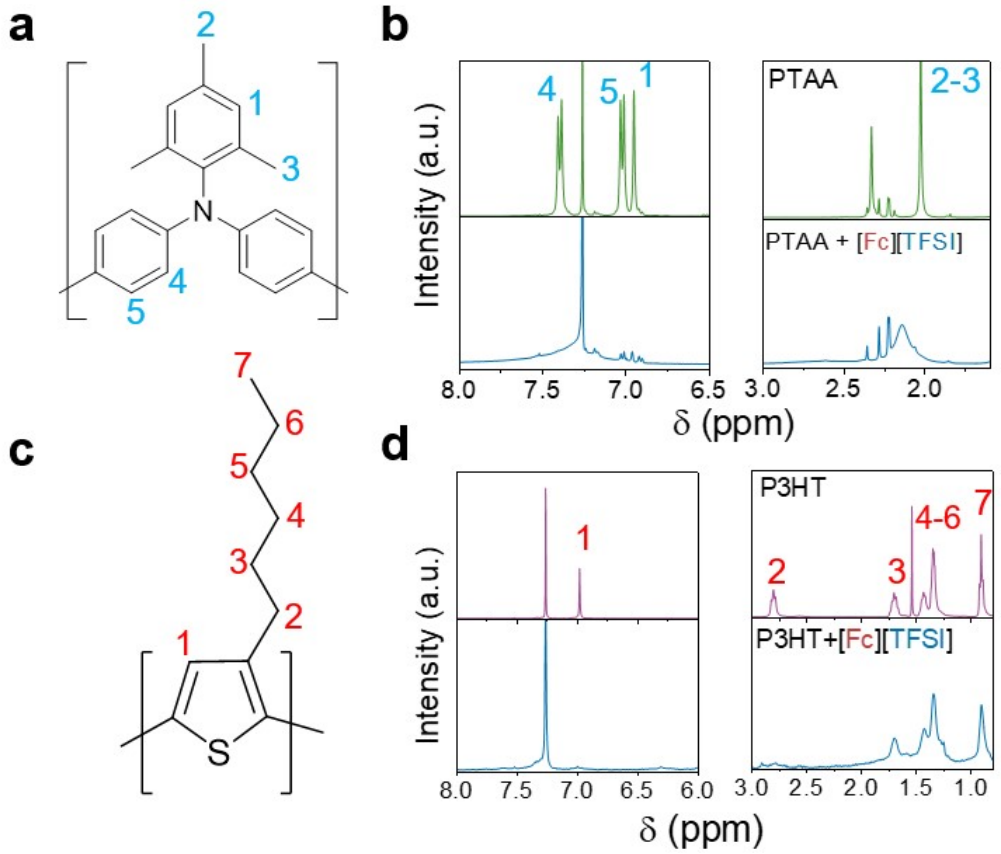

Supplementary Figure S30. ^{1}H NMR data of PTAA and P3HT before and after doping with [Fc][TFSI]. **a**, Chemical structure of PTAA and proton assignments for **b,** ^{1}H NMR spectra of PTAA before and after doping with [Fc][TFSI]. **c**, Chemical structure of P3HT with proton environments indicated. **d,** ^{1}H NMR spectra of P3HT before and after doping with [Fc][TFSI]. Oxidation of the polymer chain, like spiro-OMeTAD, leads to broadening of the peaks occurring from paramagnetic effects of the polaron. In P3HT the effects of paramagnetism on signal broadening are lessened as a function of distance down the alkyl chain from the polythiophene backbone.

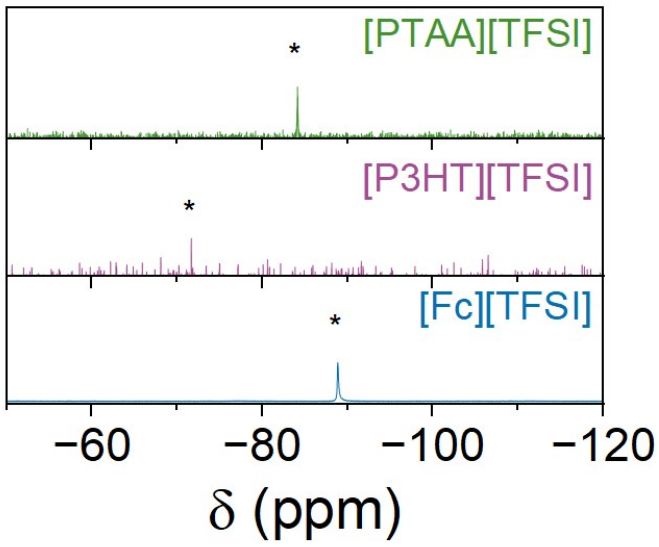

Supplementary Figure S31. ^{19}F NMR measuring the chemical environment of the TFSI anion following doping reaction with PTAA and P3HT. The formation of the new $OSC^{+}TFSI^{-}$ salt changes the chemical shift of the TFSI triflate groups as shown in the NMR. This data evidences that Equation 1 is broadly applicable to a range of OSC materials.

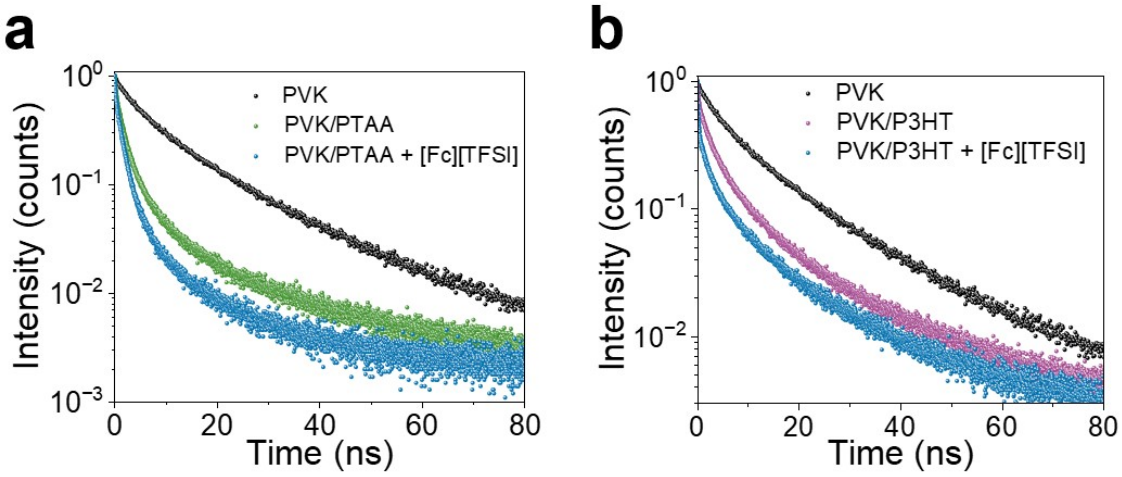

Supplementary Figure S32. Time correlated single photon counting (TCSPC) decays of perovskite films with HTLs comprising **a**, PTAA, with and without [Fc][TFSI] doping, **b**, P3HT, with and without [Fc][TFSI] doping. Perovskite excited at 404 nm, emission probed at 780 nm.

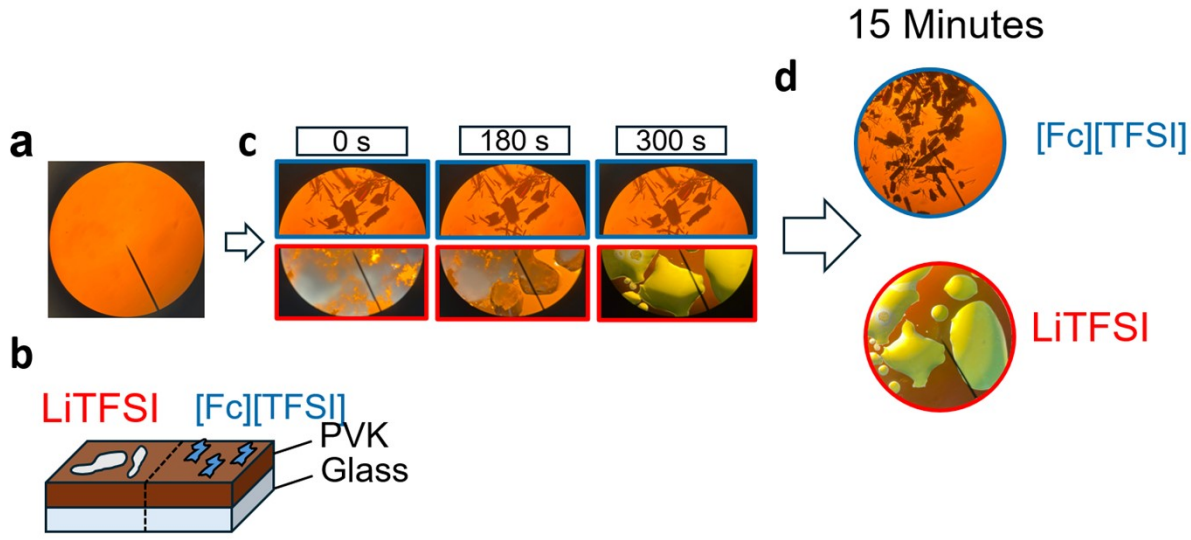

Supplementary Figure S33. Comparison of the interfacial stability of LiTFSI and [Fc][TFSI] with the perovskite interface. **a**, Microscope image of perovskite surface at 10x magnification. **b**, Schematic of the experiment on chemical stability and reactivity at the interface. **c**, Microscope images of the evolution of LiTFSI and [Fc][TFSI] dopants on the surface of perovskite as a function of storage time in ambient conditions (RH = 50 %). **d**, Microscope images of perovskite surfaces with [Fc][TFSI] and LiTFSI after a period of 15 minutes in ambient conditions.

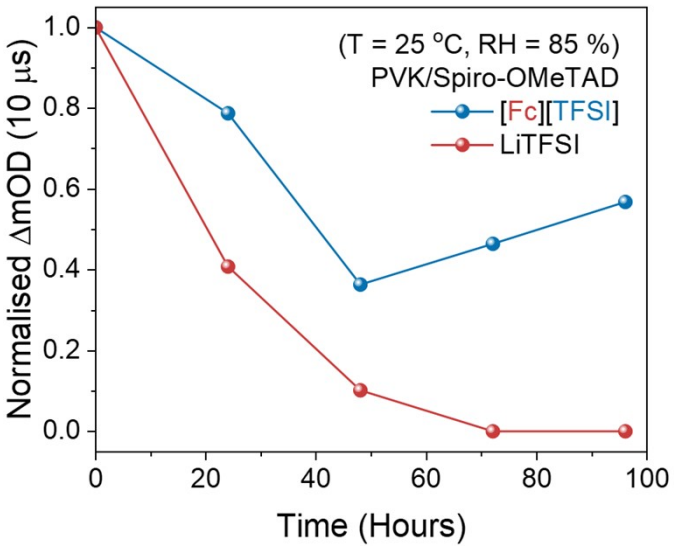

Supplementary Figure S34. Normalized ΔOD_{max} showing the change in the hole extraction yield collected from μs-TAS decays as a function of ageing times in a controlled 85 % RH humidity chamber. Samples consist of TiO_2/Perovskite/spiro-OMeTAD with either LiTFSI, tBP and FK209 dopants or [Fc][TFSI].

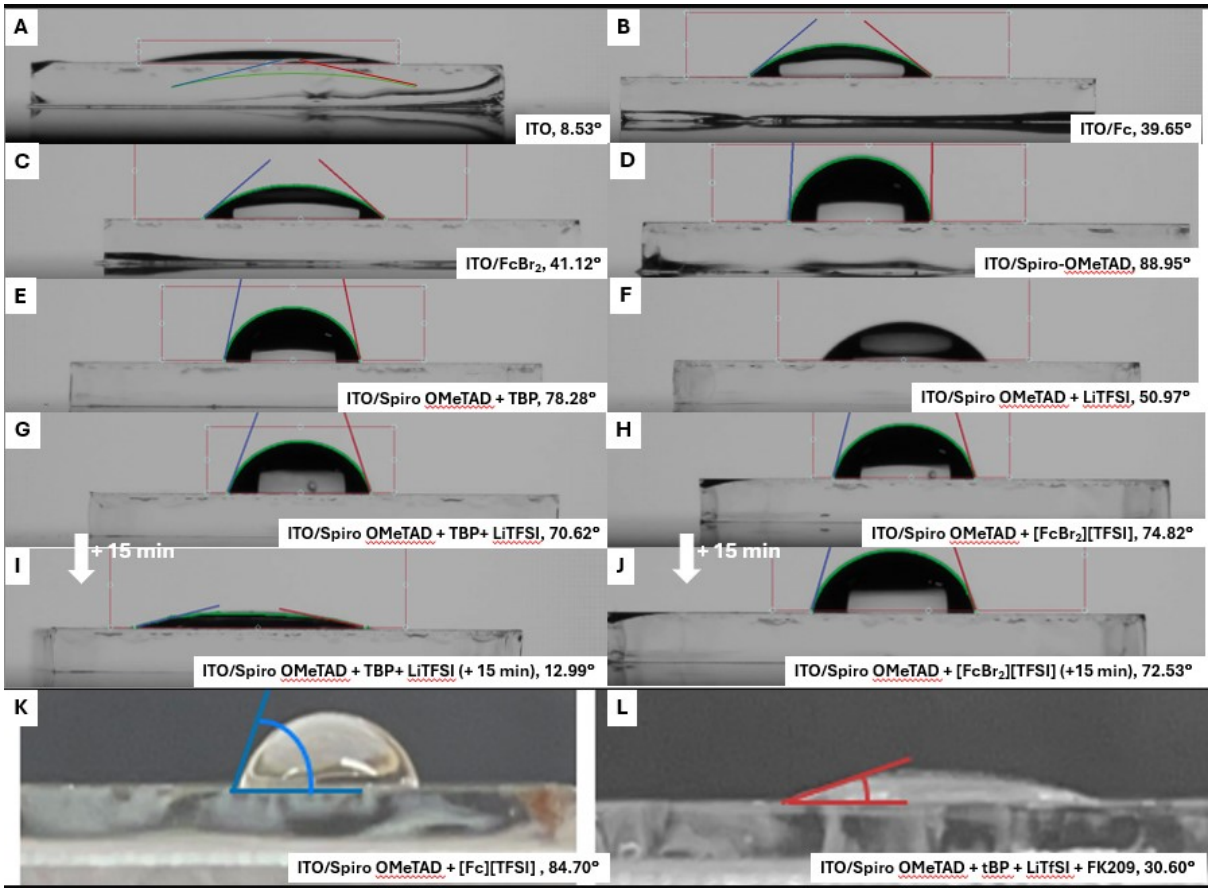

Supplementary information S35. Contact angle measurements of the angle on glass/ITO susbstrates with water droplets.

Supplementary Table S3. Contact angle values from S35

Sample ID	Average Contact Angle (degrees)
ITO	8.5
Ferrocene	39.6
Dibromoferrocene	41.1
Spiro-OMeTAD (undoped)	88.9
Spiro-OMeTAD + tBP	78.3
Spiro-OMeTAD + LiTFSI	50.9
Spiro-OMeTAD + LiTFSI + tBP	70.6
Spiro-OMeTAD + $FcBr_2$·TFSI	74.82
Spiro-OMeTAD + LiTFSI + tBP (+15 min)	12.99
Spiro-OMeTAD + $FcBr_2$·TFSI (+15 min)	72.53

FcTFSI	84.7°
LiTFSI + Fk209 + *t*BP	30.6°

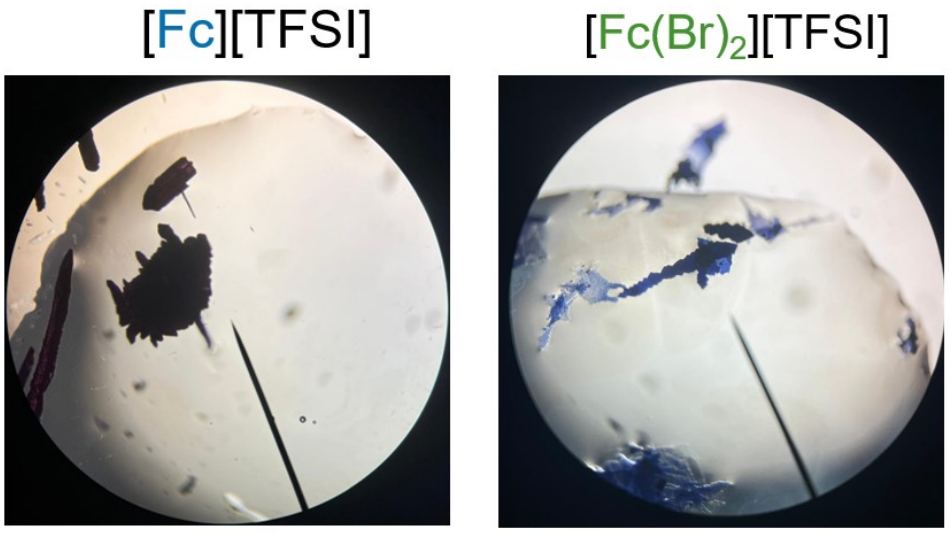

Supplementary information S36. Microscope image of [Fc][TFSI] and [Fc(Br)$_2$][TFSI] suspended in a drop of water, highlighting the excellent moisture tolerance of the ferrocenium salts.

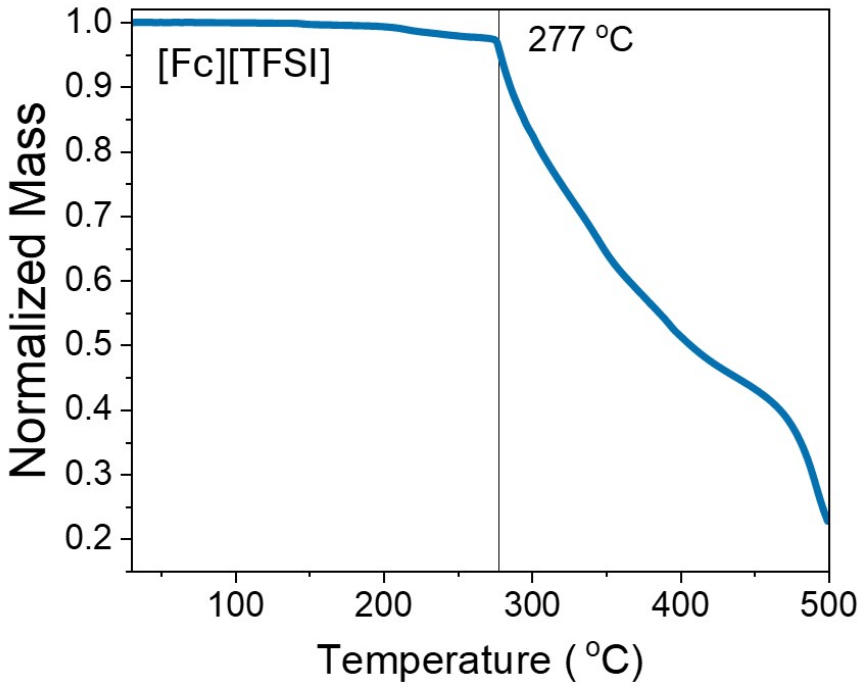

Supplementary Figure S37. Thermal Gravimetric Analysis of [Fc][TFSI] crystals. Thermal decomposition occurs at 277 °C.

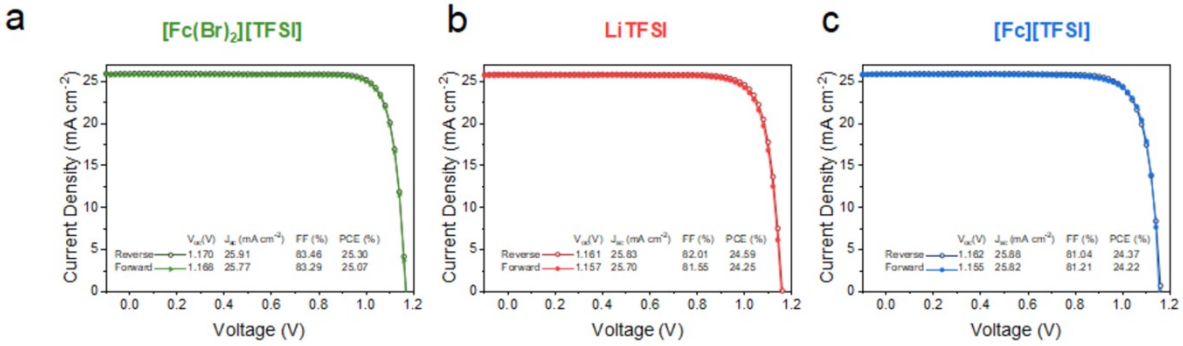

Supplementary Figure S38. Forward and reverse *J-V* data and associated parameters for champion PSCs prepared using **a**, $[Fc(Br)_2][TFSI]$, **b** LiTFSI dopant, and **c**, [Fc][TFSI].

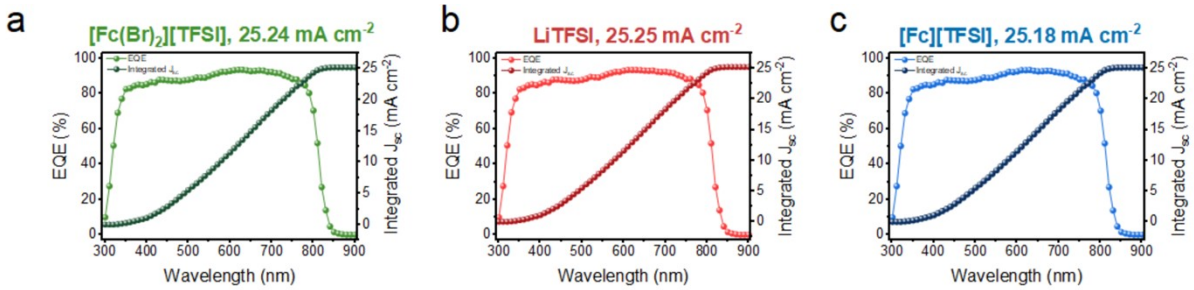

Supplementary Figure S39. External Quantum Efficiency (EQE) and integrated short circuit current density J_{sc} of PSCs prepared using **a**, $[Fc(Br)_2][TFSI]$ spiro-OMeTAD doping, **b** LiTFSI and FK209 conventional doping, **c**, [Fc][TFSI] strategies.

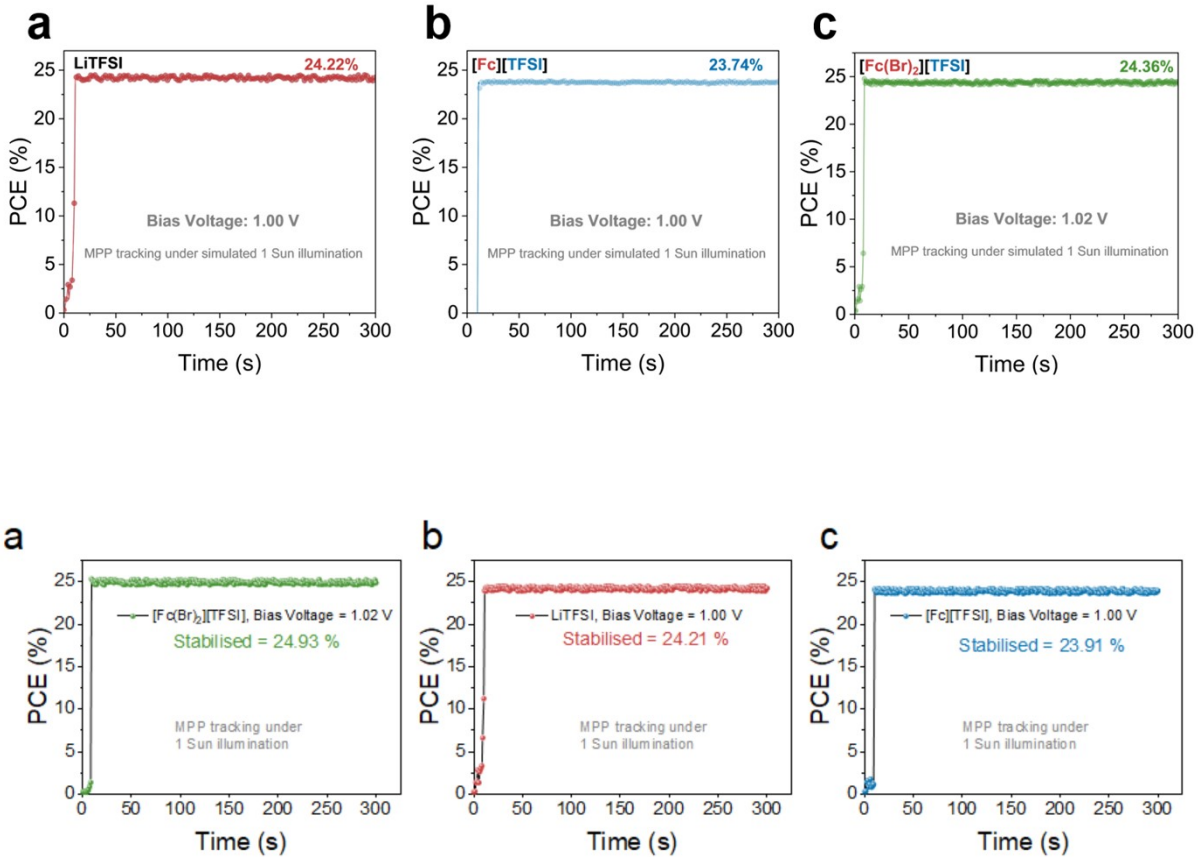

Supplementary Figure S40. Stabilised power output (SPO) measured for 300 s for PSCs prepared with **a**, $[Fc(Br)_2][TFSI]$ spiro-OMeTAD doping, **b** LiTFSI and FK209 conventional doping, **c**, [Fc][TFSI] strategies.

Supplementary note 1. Discussion of the effect of dopant on the hole kinetics and rationalisation of the -ΔOD signal recorded in TAS spectra using ferrocenium dopants.

In this work, TAS is used to probe the concentration of photogenerated holes within a hole transport layer by measuring the change in the absorbance of the spiro-OMeTAD$^{+\bullet}$ polaron. The injected photogenerated holes from the perovskite absorber increase the concentration of spiro-OMeTAD$^{+\bullet}$ within the sample. This increase in polaron concentration following excitation leads to a temporary increase to the absorbance of the sample at wavelengths at which spiro-OMeTAD$^{+\bullet}$ absorbs (λ = 1600 nm). This allows tracking of the spiro-OMeTAD$^{+\bullet}$ concentration as a function of time. These principles underpin the use of TAS to characterise the yield of hole transfer within this study.

The occurrence of a negative transient feature (-ΔOD) within the decay profile observed in **Figures 2f and 3f** indicates that the concentration of spiro-OMeTAD$^{+\bullet}$ is below the equilibrium steady-state concentration. This implies the occurrence of loss of the equilibrium spiro-OMeTAD$^{+\bullet}$ polaron concentration (doping concentration), which can be thought of as a temporary dedoping effect when doping with [Fc][TFSI] cations. We hypothesise the most likely origin of this dedoping effect is temporary hole transfer from doped spiro-OMeTAD$^{+\bullet}$ to neutral ferrocene (see Equation 1.) to temporarily reform ferrocenium species. The driving force for the equilibrium shift observed in the TAS we attribute to the high concentration of spiro-OMeTAD$^{+\bullet}$, leading to Nernst effects in the potential. This creates an additional pathway for injected holes, which occurs at a rate (k_{inj}) of ns to recombine slowly (0.1-1 ms) *via* hole transfer with Fc.

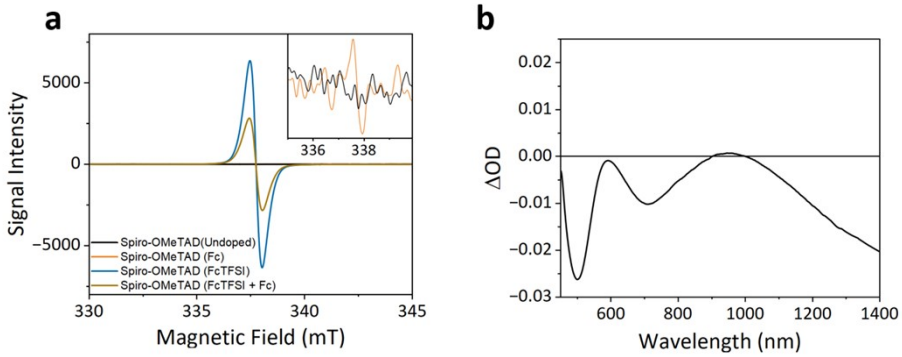

Supplementary Figure S1.1. a, EPR spectroscopy comparing the effect of Fc addition on spiro-OMeTAD doped with FcTFSI, showing a decrease in signal. (inset) Slight doping effect of the addition of ferrocene directly to spiro-OMeTAD. **b**, UV-visible absorbance spectra of the spiro-OMeTAD([Fc][TFSI])(baseline) subtracted from spiro-OMeTAD(Fc+[Fc][TFSI]).

$$\Delta OD = A_{spiro-OMeTAD(Fc+[Fc][TFSI])} - A_{spiro-OMeTAD([Fc][TFSI])}$$

To test the hypothesis that ferrocene could, at high doping concentrations, instigate an equilibrium, EPR spectra were collected of highly-doped spiro-OMeTAD with the addition of equimolar ferrocene. This data yielded 2 important points i) the presence of ferrocene following Equation 1. can limit the maximum mol% doping and, ii) ferrocene without oxidation to ferrocenium can itself encourage oxidation of spiro-OMeTAD, most likely through the effect of the noted equilibrium. The presence of such an equilibrium can be rationalised through consideration of the similar oxidation potentials of the Fc and spiro-OMeTAD, leading to Nernst dependencies on the concentrations. To confirm the presence of ferrocene as the cause of the negative spectral feature, we next replicate the spectral feature by baselining the absorbance profile of the UV-visible spectrometer to a solution of [Fc][TFSI] doped spiro-OMeTAD$^{+\bullet}$ and measuring the relative changes upon addition of ferrocene. The resultant spectra show a negative change in the absorbance in the near IR around the wavelengths measured in the TAS.

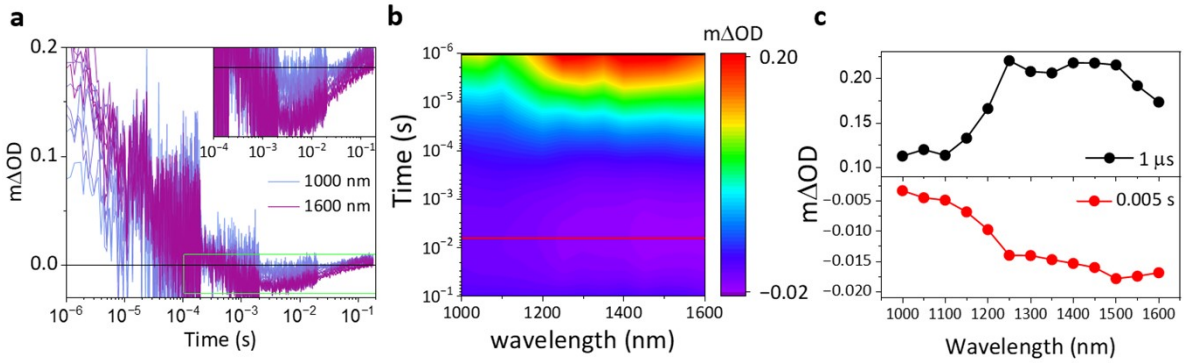

Supplementary Figure S1.2. a, Decay kinetics of the wavelength dependence scan of PVK/Spiro-OMeTAD interface doped with [Fc][TFSI]. **b**, 3D contour map of the ΔOD values of the decays presented in **a**, showing a gradual increase in the negative photobleach as the wavelength is increased towards the IR region. **c**, Linecuts of the 3D contour maps taken at lifetimes of 1 µs (Spiro-OMeTAD$^{+\bullet}$) and 0.005 s (unknown negative photobleach). The figure shows symmetry between the new negative spectral feature and the profile associated with the transient feature of the spiro-OMeTAD polaron.

To match the UV-visible absorbance spectra to the negative features observed in the TAS we measured additional TAS as a function of wavelength as shown in **Supplementary Figure S1.2 a**. These decays were then converted to a 3D heat map of spiro-OMeTAD$^{+\bullet}$ absorbance intensity as a function of wavelength, where the dedoping of spiro-OMeTAD$^{+\bullet}$ is purple and occurs on timescales of 10^{-3} to 10^{-1} s (**Supplementary Figure S1.2b**. Taking 1D linecuts of the spectra at 1×10^{-6} and 5×10^{-3}, corresponding to the maximum yield of hole transfer and the maximum of the negative feature, we confirm that the new feature exhibits the same spectral

dependence as the spiro-OMeTAD$^{+\bullet}$ following hole injection but inverted, consistent with a decrease in the concentration of holes. Furthermore, this feature matches the spectral shape given in **Supplementary Figure S1.2c**, further confirming an additional slow, temporary dedoping effect as a recombination mechanism on the order of seconds.

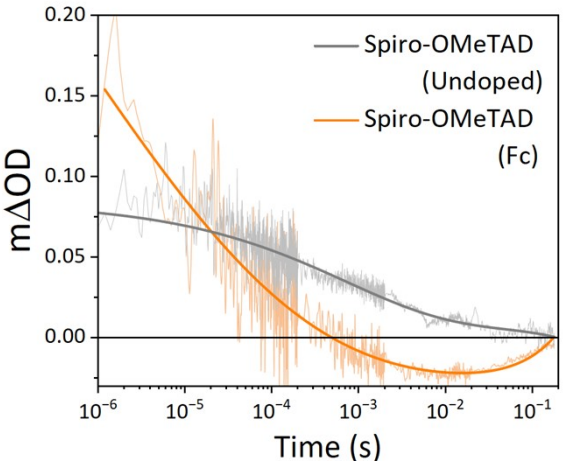

Supplementary Figure S1.3 TAS decays of undoped spiro-OMeTAD with and without ferrocene.

Finally, an exaggerated concentration of ferrocene 15 mol % was added to undoped spiro-OMeTAD and the TAS experiment was repeated (**Supplementary Figure S1.3**). Compared to the undoped spiro-OMeTAD decay, we observe a significant change in the decay dynamics consistent with our previous findings to this point.

a

$$\frac{d[Spiro^+]}{dt} = k_{inj}[Spiro^+] - \overbrace{k_{recom}[Spiro^+]}^{\sim 1\mu s - 1\ ms}$$

b

$$\frac{d[Spiro^+]}{dt} = k_{inj}[Spiro^+] - \overbrace{k_{recom}[Spiro^+]}^{\sim 1\mu s - 1\ ms} - \overbrace{k_{Fc(1)}[Spiro^+]}^{\sim 1\mu s - 1\ ms} + \overbrace{k_{Fc^+(2)}[Spiro^+]}^{\sim 0.01s}$$

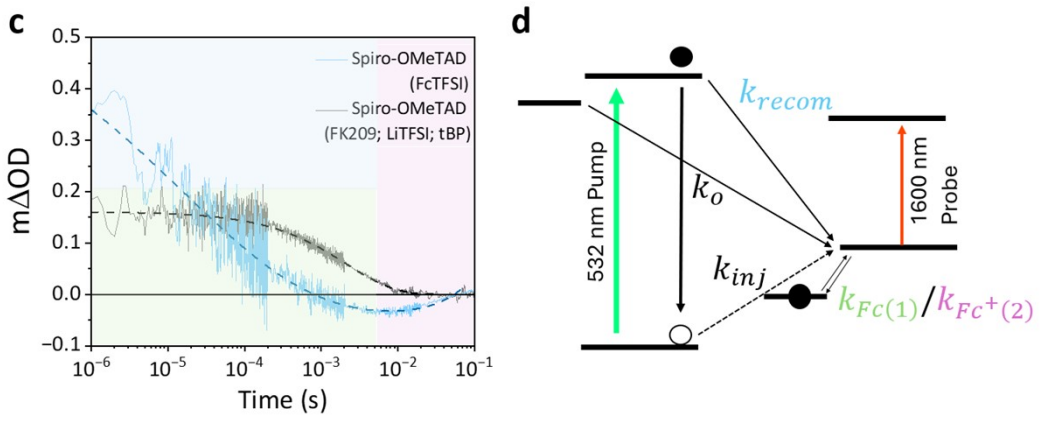

Supplementary Figure S1.4. Modified charges in the kinetics of spiro-OMeTAD polaron when using dopants of a similar oxidation potential to the first ionisation potential of spiro-OMeTAD. **a**, classic generalised interpretation of the changes in spiro-OMeTAD polaron population, consisting of injection from the absorber and recombination with either the absorber CB or ETL CB. **b**, proposed modified kinetics of spiro-OMeTAD polaron population, including transient dedoping and doping terms. **c**, Annotated TAS decays showing the region at which different kinetic processes dominate. **d**, Schematic of modified hole kinetics in systems with a hole acceptor in close energetic proximity to the first oxidation state of spiro-OMeTAD.

Using these findings, we propose a new set of kinetics to describe the use of additives where the oxidation potential between an extrinsic species and the OSC is energetically close, such as ferrocenium. These kinetics may extend more widely beyond the use of ferrocenium-specific species to scenarios where a hole-accepting species or semiconductors which have a close energetic proximity to the first ionisation potential of spiro-OMeTAD.

In a conventional system, the change in the concentration of spiro-OMeTAD$^{+\bullet}$ is given by **Supplementary Figure S1.4a** and involves a picosecond hole injection process (k_{inj}) and a slower interfacial recombination process (k_{recom}) with electrons provided by either the absorber CB or the ETL (**Supplementary Figure S1.4d**). The TAS decays indicate that 2 new processes occur that i) remove additional spiro-OMeTAD$^{+\bullet}$ beyond that of the equilibrium doping level and ii) a recovery to the steady-state doping equilibrium. In the case of the latter, this observation provides an approximate timescale for the doping reaction between spiro-OMeTAD and the ferrocenium salts, suggesting that hole transfer occurs on a sub-second timescale. Given the fast redox chemistry of the Fc/Fc$^+$ half-cell as frequently reported, this is likely a diffusion-governed rate.

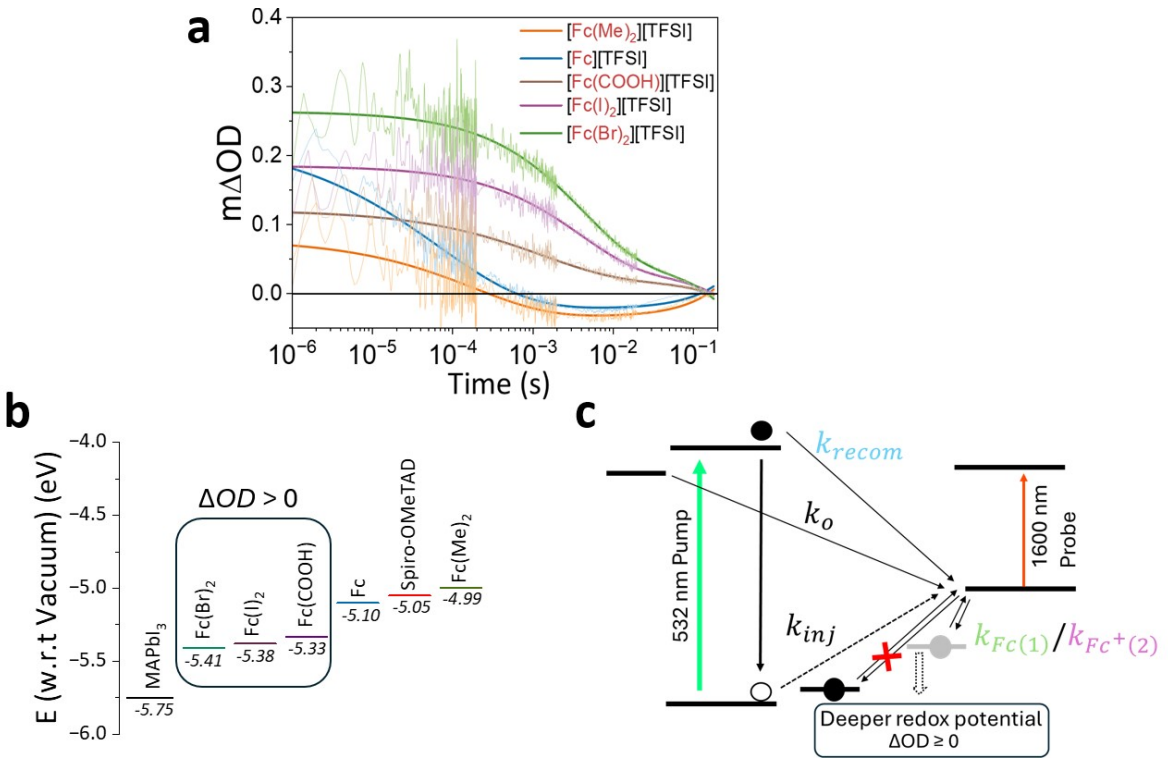

Supplementary Figure S1.5. Application of proposed kinetics to the observations made upon changing the functional groups of the ferrocenium compounds. **a**, TAS decays of spiro-OMeTAD doped with different ferrocenium derivatives. **b**, Comparison of the energetic potential of the HOMO state used for doping / hole transfer. **c**, Schematic of the modified hole kinetics at the absorber / spiro-OMeTAD interface highlighting the benefits of deepening the potential of the ferrocenium species.

We next use this model to rationalise the difference in decays presented in **Figure 3f**. Negative transient features associated with the temporary dedoping are observed in samples prepared using [$Fc(Me)_2$] and [Fc] cations, with the behaviour being most pronounced in the case of the former. The absence of the signal in [Fc(COOH)], [$Fc(I)_2$] and [$Fc(Br)_2$] can be rationalised through consideration of the energetic potentials as shown in **Supplementary Figure S1.5b**. In the case of the deeper lying ferrocenium-based cations, the creation of an energetic barrier to the hole from transferring back to the dopant. As such, the dedoping process is deactivated and the negative feature is not observed. We note a detailed discussion of these kinetics on device performance is beyond the scope of this work, but highlight that these processes occur on timescales typically longer than reported values of hole extraction from an HTL into a metal electrode, which is typically reported to occur on a timescale of between 1 – 10 μs. Nevertheless, the ability of the design of the dopant to influence the hole kinetics is important design criteria, whereby some device improvement can be expected upon removal of the dedoping pathway.

References

1. Connelly, N. G. & Geiger, W. E. Chemical Redox Agents for Organometallic Chemistry. *Chem. Rev.* **96**, 877–910 (1996).

2. Khobragade DA, Mahamulkar SG, Pospíšil L, Císařová I, Rulíšek L, Jahn U. Acceptor-Substituted Ferrocenium Salts as Strong, Single-Electron Oxidants: Synthesis, Electrochemistry, Theoretical Investigations, and Initial Synthetic Application. Chemistry–A European Journal. 2012 Sep 24;18(39):12267-77.